Published in Applied Energy with doi: 10.1016/j.apenergy.2024.123067
© 2024. This manuscript version is made available under the CC-BY-NC-ND 4.0 license
https://creativecommons.org/licenses/by-nc-nd/4.0/

An ADMM-Enabled Robust Optimization Framework for Self-Healing Scheduling of Smart Grids Integrated with Smart Prosumers

Pan Zhang[1], Seyed Amir Mansouri[2*], Ahmad Rezaee Jordehi[3], Marcos Tostado-Véliz[4], Yahya Z. Alharthi[5], Murodbek Safaraliev[6]

[1] School of Mathematical Sciences, Anhui University, Hefei 230601, China
[2] Institute for Research in Technology (IIT), ICAI School of Engineering, Comillas Pontifical University, 28015 Madrid, Spain
[3] Department of Electrical Engineering, Rasht Branch, Islamic Azad University, Rasht, Iran
[4] Department of Electrical Engineering, University of Jaén, 23700 Linares, Spain
[5] Department of Electrical Engineering, College of Engineering, University of Hafr Albatin, Hafr Al Batin 39524, Saudi Arabia
[6] Department of Automated Electrical Systems, Ural Federal University, 620002 Yekaterinburg, Russia

Abstract

Enhancing the reliability of energy networks and minimizing downtime is crucial, making self-healing smart grids indispensable for ensuring a continuous power supply and fortifying resilience. As smart grids increasingly incorporate decentralized prosumers, innovative coordination strategies are essential to fully exploit their potential and improve system self-healing capabilities. To address this need, this paper presents a novel bi-level strategy for managing the self-healing process within a smart grid influenced by Hydrogen Refueling Stations (HRSs), Electric Vehicle Charging Stations (EVCSs), and energy hubs. This approach taps into the combined potential of these prosumers to boost system self-healing speed and reliability. In the initial stage, the Smart Grid Operator (SGO) conducts self-healing planning during emergencies, communicating required nodal capacities to prevent forced load shedding and outlining incentives for smart prosumers. Subsequently, prosumers schedule their activities and contribute flexible capacities to the SGO. Bridging the first and second stages, an adaptive Alternating Direction Method of Multipliers

[*] Corresponding Author: smansouri@comillas.edu & amir.mansouri24@gmail.com

(ADMM) algorithm ensures convergence between the SGO and prosumer schedules within a decentralized framework. This strategy underwent implementation on a 118-node distribution system using GAMS. Results demonstrate that the proposed concept reduces Forced Load Shedding (FLS) by 32.04% and self-healing costs by 17.48% through effective utilization of smart prosumers' flexible capacities. Furthermore, outcomes indicate that the SGO reduces FLS by 6.69% by deploying Mobile Electrical Energy Storages (MEESs) and Mobile Fuel Cell Trucks (MFCTs) to critical nodes.

Keywords: Smart Grids; Self-Healing; Energy Hubs; Hydrogen Energy; Vehicle-to-Grid Services; Alternating Direction Method of Multipliers.

Nomenclature

Abbreviations	
ADMM	Alternating Direction Method of Multipliers
CHP	Combined Heat and Power
DER	Distributed Energy Resource
DLC	Direct Load Control
DR	Demand Response
EES	Electrical Energy Storage
EHP	Electric Heat Pump
EV	Electric Vehicle
EVCS	Electric Vehicle Charging Station
FCV	Fuel Cell Vehicle
FLS	Force Load Shedding
HRS	Hydrogen Refueling Stations
IGDT	Information Gap Decision Theory
LC	Load Control
MEES	Mobile Electrical Energy Storages
MFCT	Mobile Fuel Cell Trucks
MILP	Mixed-Integer Linear Programming
RES	Renewable Energy Source
SGO	Smart Grid Operator
WF	Wind Farm
Sets	
c	Connection point index
g	DER index
e	EES index
h	Energy hub index
v	EV/FCV index
p	EVCS index
s	HRS index
n	MEES index
m	MFCT index

t	Time index
Scalar	
Δt	Time gap (h)
η_{hc}^{AC}	Absorption chiller efficiency (%)
η^{PV}	PV panel efficiency (%)
η^{GT}	Gas turbine efficiency (%)
η_{gh}^{Boiler}	Boiler efficiency (%)
$\eta_{eh}^{EHP} / \eta_{ec}^{EHP}$	Heating/Cooling efficiency of EHP (%)
η^{Ch} / η^{Dch}	Charging/Discharging efficiency of storage systems (%)
L^{H_2}	Low heat value of hydrogen (kJ/kg)
M	Positive big number
π^{S}	Operation cost of EES ($/kW)
R_{stc}	Sun irradiance for STC (kW/m^2)
$v^{r} / v^{co} / v^{ci}$	Rate/Cut-Out/Cut-In speed (m/s)
Parameters	
$a_h^{CHP} / b_h^{CHP} / c_h^{CHP} / d_h^{CHP} / e_h^{CHP}$	Coefficient of CHP gas consumption function
$\alpha_{ij,0}^{F}$	Initial status of network switched
$C_{h,t}^{AC,\max}$	AC capacity (kW)
C_b^{L} / C_b^{D}	LC cost ($/kW)
C_s^{El}	Operation cost of electrolyzer ($/kW)
$D_{q,r}$	Distance between travelling points (m)
$E_h^{\min,EES/TES/CES} / E_h^{\max,EES/TES/CES}$	Energy of storage system (kWh)
$E_h^{In,EES/TES/CES}$	Initial energy of storage system (kWh)
$E_n^{\max}$	MEES capacity (kWh)
η_n^{Dch}	Efficiency of MEES converter (%)
η_s^{FC}	Fuel cell efficiency (%)
$H_m^{In,\max}$	Maximum loading capacity of MFCT (kg)
$H_m^{MFCT,\max}$	MFCT tank capacity (kg)
$H_h^{Boiler,\max}$	Boiler capacity (kW)
$H_{s,t}^{Load}$	Hydrogen load of HRS (kg)
$H_s^{HRS,\min} / H_s^{HRS,\max}$	Minimum/maximum HRS tank capacity (kg)
$\varphi_h / \varphi_p / \varphi_s$	Active-to-reactive power ratio of smart prosumers
$\lambda_{h,t}^{E} / \lambda_{p,t}^{E} / \lambda_{s,t}^{H}$	Daul coupling variables of smart prosumers ($/kW-$/kg)
$P_{v,t}^{Ch,\max} / P_{v,t}^{Dch,\max}$	Maximum charging/discharging level of EV (kW)
$P_h^{EHP,\max}$	EHP capacity (kW)
$P_m^{FC,\max}$	Fuel cell capacity (kW)
$P_n^{Dch,\max}$	Maximum discharging level of MEES (kW)
$P_{s,t}^{HRS}$	Power consumption of HRS at normal conditions (kW)
$P_{p,t}^{EVP}$	Power consumption of EVCS at normal conditions (kW)
$P_{h,t}^{Hub} / G_{h,t}^{Hub}$	Power/Gas consumption of energy hub at normal conditions (kW)
P_g^{Rate}	Rate power of RES (kW)
$P_{g,t}^{PV}$	PV system power output (kW)
$P_{g,t}^{WT}$	Wind farm power output (kW)

$P_i^{L,\max} / Q_i^{L,\max}$ Active/Reactive load of network buses (kW/kVAR)

$P_i^{S,\max} / Q_i^{S,\max}$ Maximum active/reactive power exchange with upstream grid (kW/kVAR)

$P_g^{GT,\min} / P_g^{GT,\max}$ Minimum/maximum active power generation of gas turbine (kW)

$Q_g^{GT,\min} / Q_g^{GT,\max}$ Minimum/maximum reactive power generation of gas turbine (kVAR)

π_i^L Penalty of load shedding ($/kW)

π_{ij}^F Switching cost ($)

π_t^{UG} upstream network energy price ($/kWh)

π_n^{Tr} / π_m^{Tr} Travelling cost of MEES/MFCT ($/m)

π_t^G Gas price ($/kW)

$\pi_{h,t}^E / \pi_{p,t}^E / \pi_{s,t}^E$ Energy price at coupling nodes of smart prosumers ($/kWh)

π_t^H Hydrogen price ($/kg)

R_t Sun irradiance (kW/m^2)

r_{ij} Line resistance (ohm)

r^{it} / d^{it} Primal/Daul residuals

ρ^{it} Penalty factor ($/kW)

$S_{ij}^{F,\max}$ Line capacity (kVA)

$T_{q,r}$ Travelling time (h)

v_t Wind speed (m/s)

$V_i^{B,\min} / V_i^{B,\max}$ Square of minimum/maximum voltage limit (V^2)

$\upsilon_b^L / \upsilon_b^D$ LC level (%)

Variables

a Transformer tap

$C_{h,t}^{AC}$ AC cooling generation (kW)

$E_{h,t}^{EES/TES/CES}$ Energy of storage systems (kWh)

$G_{h,t}^{CHP}$ CHP gas consumption (kW)

$G_{h,t}^{Boiler}$ Boiler gas consumption (kW)

$H_{s,m,t}^{Buy}$ Hydrogen input of MFCT (kg)

$H_{c,m,t}^{FC}$ Hydrogen output of MFCT (kg)

$H_{m,t}^{MFCT}$ Hydrogen level in MFCT tank (kg)

$H_{h,t}^{Boiler}$ Boiler Heating generation (kW)

$H_{h,t}^{AC}$ AC Heating consumption (kW)

$H_{h,t}^{EHP} / C_{h,t}^{EHP}$ EHP heating/cooling generation (kW)

$H_{s,t}^{HRS}$ Hydrogen level in HRS tank (kg)

$H_{s,t}^{El}$ Electrolyzer hydrogen generation (kg)

$H_{v,t}^{Ch,FCV}$ Fuel cell hydrogen consumption (kg)

$n_{ij,t}^{Tap}$ Tap number

$P_{h,t}^{EHP}$ EHP power consumption (kW)

$P_{c,n,t}^{Dch,MEES} / P_{c,m,t}^{Dch,MFCT}$ Discharging power of MEES/MFCT (kW)

$P_{h,t}^{Ch,EES/TES/CES} / P_{h,t}^{Dch,EES/TES/CES}$ Charging/Discharging power of storage systems (kW)

$P_{h,t}^{Em,Hub} / P_{p,t}^{Em,EVP} / H_{s,t}^{Em,Sell}$ Participation level of smart prosumers in emergencies (kW)

$P_{i,t}^S / Q_{i,t}^S$ Active/Reactive power exchange level of upstream network (kW/kVAR)

$P_{ij,t}^{F} / Q_{ij,t}^{F}$	Active/Reactive power flow of line (kW/kVAR)
$P_{i,t}^{L} / Q_{i,t}^{L}$	Active/Reactive level of supplied load (kW/kVAR)
$P_{g,t}^{GT} / Q_{g,t}^{GT}$	Active/Reactive power generation by gas turbine (kW/kVAR)
$P_{h,t}^{CHP} / H_{h,t}^{CHP}$	CHP power/heat generation (kW)
$P_{v,t}^{Ch,EV} / P_{v,t}^{Dch,EV}$	charging/Discharging power of EV (kW)
$P_{s,t}^{El}$	Electrolyzer power consumption (kW)
$V_{i,t}^{B}$	Squar value of voltage magnitude (V^2)
Binary Variables	
$\alpha_{ij,t}^{F}$	Status of line switch
$\beta_{ij,t}^{F} / \beta_{ji,t}^{F}$	Status of parent nodes
$u_{r,m,t}^{MFCT}$	Status of MFCT traveling point
$x_{v,t}^{EV}$	EV charging stratus
$x_{i,t}^{L}$	Status of load supply level
$x_{i,t,b}^{LC} / x_{h,t,b}^{Z}$	Status of DLC level
$x_{c,n,t}^{MEES}$	Status of MEES location
$x_{h,t}^{EES/TES/CES}$	Storage systems charging status
$x_{r,m,t}^{MFCT}$	Status of MFCT location
$x_{0,m,t}^{MFCT}$	Status of MFCT location in normal or traveling conditions
$x_{h,t}^{CHP}$	Stats of CHP operation point
$x_{h,t}^{EHP}$	Stats of EHP operation mode
$x_{v,t}^{FCV}$	FCV charging stratus

1. Introduction

1.1. Context and Motivation

Modern society demands a power system characterized by exceptional reliability, scalability, security, interoperability, and manageability, all while maintaining cost-effectiveness. In line with the Horizon Europe 2021–2027 vision, the future electric power system is envisioned as a smart grid, characterized as a grid with self-healing capabilities, ensuring dependable, energy-efficient, and high-quality power supply [1]. Smart grids can be classified into transmission and distribution systems based on their functions. In a transmission system, electricity components form a ring network, supported by multiple power supply generators. Therefore, the failure of a single component has a minimal impact on the transmission network's operation. Conversely, the distribution system has a radial structure, delivering electricity directly to customers. Even a minor

failure in the distribution system can significantly degrade service quality (QoS) for individual customers [2].

Self-healing capability is crucial for a smart grid, ensuring that faulty components are isolated from the grid, and the system can autonomously return to normal operation without human intervention. A self-healing-capable grid can prevent or reduce power supply interruptions, minimize restoration time, and maximize the load during restoration, maintaining system reliability and availability. It is widely recognized that proactive measures like sectionalizing the smart grid into islanded microgrids, implementing load control programs, and dispatching mobile emergency resources effectively enhance resilience and enable self-healing in smart grids with distributed generators [3,4].

Smart prosumers, like energy hubs, play a pivotal role in enhancing self-healing capabilities within smart grids. By integrating various energy resources, such as renewable generation, storage, and demand response (DR), energy hubs optimize energy usage and grid stability. During outages or disturbances, energy hubs can disconnect from the main grid, operate independently, and even provide essential power to critical loads. Their flexibility in managing distributed energy resources aids in grid restoration, ensuring continuous power supply to consumers [5–7].

Self-healing can be achieved through both centralized and decentralized strategies. Centralized self-healing relies on a central control center for grid management and decision-making, while decentralized self-healing distributes decision-making and control functions across local controllers and devices. Decentralized self-healing excels in resilience, adaptability, and reliability, reducing dependence on a central control center and enhancing grid performance in diverse conditions, making it a priority for modern smart grids [8,9].

Recently, hydrogen energy is gaining prominence as a solution to address environmental issues and facilitate the decarbonization process, attracting global attention in recent years. The integration of hydrogen energy and its related infrastructure into energy systems not only facilitates the incorporation of intermittent renewables like wind and solar power but also enhances operational flexibility. With the rapid growth of hydrogen energy, its penetration in the power, energy, and transportation sectors has surged. It is inevitable that some smart grids will integrate hydrogen energy and its associated infrastructure in the near future. In hydrogen-penetrated smart grids, hydrogen energy and related facilities can serve as backups or alternatives, aiding in restorative self-healing and bolstering the grid's resilience during extreme events.

The descriptions above have motivated us to design a bi-level self-healing strategy for smart grids, leveraging the potential of smart prosumers to enhance system resilience during fault conditions. The increasing integration of hydrogen-related facilities in distribution systems in recent years has also encouraged us to harness the potential of hydrogen-based facilities, especially HRSs and MFCTs, to facilitate system self-healing. Lastly, recognizing the significance of prosumer privacy, we have introduced an adaptive ADMM algorithm to ensure coordination between the SGO and smart prosumers within a decentralized environment, with minimal information sharing.

1.2. Literature Review

Recent research has made significant strides in developing advanced optimization techniques for self-healing planning in smart grids. These efforts aim to enhance grid resilience, minimize downtime, and optimize fault detection and recovery, ultimately ensuring more reliable and efficient electrical systems. In this context, [10] conducted a comprehensive review of existing articles in the field of self-healing distribution systems, categorizing them based on optimization objectives, control measures, and solution algorithms. The authors of this research emphasized the

benefits of implementing self-healing in modern distribution networks. In [11], a blockchain-based P2P framework for planning self-healing microgrids under cyber attacks was presented. This framework includes a predictive control model aimed at reducing denial-of-service attacks and network delays. The results demonstrated the proposed framework's ability to quickly identify cyber attacks and optimize self-healing strategies. [12] introduced a strategy based on multi-agent concept for self-healing management of smart grids, highlighting the role of zone agents in fault condition awareness. This strategy encompasses fault location, fault area isolation, fault-tolerant mechanism implementation, and system recovery. Implementation on a 71-bus smart grid confirmed its accuracy in fault identification and system reorganization speed. [13] presented a model based on multi-agent concept, considering faults in network power distribution. The model leverages the potential of various agents to enhance self-healing quality and speed. [14] introduced a novel multi-agent algorithm for planning self-healing in smart grids within a decentralized space with minimal data sharing. Simulation results demonstrated increased system stability and reliability while preserving stakeholder privacy.

Additionally, several studies have centered around utilizing the ADMM algorithm for self-healing planning in distribution systems. In [15], a distributionally optimization model for self-healing management of distribution systems was presented, utilizing the ADMM technique. This research addressed computational challenges arising from increased decision variables, integrating a clustering technique with the ADMM algorithm to reduce calculations and enhance self-healing problem-solving speed. [16] introduced a hierarchical structure for self-healing system management using the ADMM algorithm, with a focus on ensuring stakeholder privacy and reducing computational complexity. Local controllers manage recovery operations for each fragmented area, coordinated via the ADMM algorithm. The authors in [17] also designed their

self-healing strategy based on the ADMM algorithm, emphasizing decentralized optimization of different parts of a 33-bus electrical network while involving all stakeholders. [18] utilized the ADMM algorithm for decentralized coordination of different distribution system components under emergency conditions, without central control. This strategy, formulated as Mixed Integer Quadratically Constrained Programming (MIQCP), demonstrated its effectiveness in enhancing system reliability and recovery speed. An evaluation of these research works reveals that many self-healing strategies based on the ADMM algorithm primarily focus on coordinating islanded network segments, rather than proactively coordinating smart prosumers and harnessing their capabilities.

Recent research endeavors have diligently explored the integration of electrical- and hydrogen-based energy storage solutions to bolster the effectiveness of self-healing planning within distribution systems. These efforts aim to fortify grid resilience, mitigate downtime, and optimize fault detection and recovery mechanisms, fostering more robust and reliable distribution networks. In this regard, [19] introduced a two-layer optimization strategy for self-healing smart grids, utilizing electric and hydrogen storage systems to support critical loads during emergency conditions. The strategy employs the Information Gap Decision Theory (IGDT) technique to manage uncertainties, categorizing them as normal, non-critical, or critical. Simulation results demonstrate the significant impact of electric and hydrogen storage in preventing critical load shedding. In [3], a self-healing strategy is developed based on the Generic Microgrid Controller (GMC) concept, prioritizing the prevention of critical load interruptions during emergencies. Modeled as a Mixed-Integer Linear Programming (MILP) problem, case studies affirm its effectiveness in harnessing the capacities of electric, thermal, and hydrogen storage systems to safeguard sensitive loads and facilitate system self-healing.

Additionally, several studies have focused on leveraging mobile energy storage units to enhance distribution system self-healing. [20] introduced a two-layer model for self-healing management of hydrogen-penetrated distribution systems, incorporating MEESs and HRSs. In this model, the system operator deploys MEESs to islanded areas to avert critical load disruptions in emergency scenarios. Moreover, HRSs utilize fuel cells to convert hydrogen into electricity during emergencies, preventing load shedding. Similarly, [21] presented a two-level model that integrates MEESs into a 33-bus distribution system for self-healing purposes. The primary objective of the first level is to minimize load shedding during emergencies, while the second level focuses on maintaining voltage within a safe range. Case studies demonstrate that MEES deployment not only reduces load shedding but also significantly improves voltage stability. In [22], the battery capacity of electric buses (EBs) is harnessed to enhance network self-healing during emergencies. The research findings indicate that active participation of EBs in the self-healing process reduces load shedding in fault-affected areas by approximately 64%.

Many research papers have highlighted the significance of load control (LC) programs as a crucial tool for bolstering self-healing capabilities in distribution systems. In this context, [23] introduced a self-healing strategy incorporating programs, utilizing the capacities of d (DERs) and flexible loads to maintain voltage stability during emergencies and facilitate system self-healing. Case study results indicate that LC programs have improved system stability by approximately 30%. In [24], a centralized self-healing strategy was proposed, emphasizing the utilization of Electric Vehicles (EVs) and LC programs for system recovery during emergencies. Research outcomes demonstrate that redistributing loads through LC programs has substantially reduced forced load shedding in the network. Additionally, modifying EV charging schedules during emergencies enhances operational flexibility and expedites system recovery. [25] presented a comprehensive

self-healing distribution system planning strategy, leveraging LC programs to prevent critical load shedding during emergencies. Implementation of this strategy on a 39-bus distribution system has proven effective in enhancing resilience and significantly reducing operational costs.

Recent research has increasingly emphasized harnessing the potential of smart prosumers, such as energy hubs, energy communities, and internet data centers, to enhance the self-healing capabilities of distribution systems. In [26], a two-layer optimization framework for self-healing in intelligent systems is introduced, utilizing the capabilities of smart prosumers, particularly internet data centers, for system recovery. This model is decentralized to protect internet data centers' privacy. Simulation results demonstrate that internet data centers participation in the self-healing process effectively prevents critical load disruptions. In [27], the authors considered multi-energy communities as smart prosumers, employing them for network restoration during emergencies. Research findings confirm that multi-energy communities, equipped with internal converters like Combined Heat and Power (CHP) and boilers, provide valuable flexibility to the system operator, reducing load shedding. [28] presents a four-stage optimization framework for self-healing planning, leveraging smart prosumers, notably photovoltaic (PV)-integrated buildings and electric vehicle (EV) parking lots, to facilitate system recovery during emergencies. The study reveals that unlocking the capacities of smart buildings and EV parking lots leads to a 93% reduction in load shedding and a subsequent 49% cost reduction. In [29], a two-stage self-healing model for a 118-bus distribution system is proposed, with energy hubs acting as smart prosumers. The strategy employs DFR and Load Curtailment (LC) programs to expedite system recovery during emergencies. Simulation results in GAMS indicate that energy hubs provide substantial capacities to the system operator by adjusting their plans during emergencies. Additionally, their participation in the self-healing process, along with the utilization of various storage systems,

prevents pressure drops in the gas network. Furthermore, [30] investigates the role of CHP units in enhancing operational flexibility during emergency conditions. Several case studies demonstrate the positive impact of CHP units on system flexibility and resilience. Lastly, [31] presents a self-healing strategy for multi-carrier systems equipped with multi-generation converters and electrical, thermal, and cooling storage systems. The strategy is modeled using MILP formulation, revealing the substantial effect of multi-generation converters and storage systems in improving resilience and reducing system costs during emergencies.

1.3. Research Gap and Contributions

The literature review illuminates a significant research void in the realm of orchestrating decentralized smart prosumers within the realm of self-healing planning. While previous studies have made commendable strides, they predominantly fixated on dissecting specific facets in isolation, leaving a conspicuous absence of comprehensive models that embrace the holistic interplay of energy hubs, EVCSs, and HRSs. Moreover, the exploration of leveraging the ADMM algorithm to unleash flexible capacities via enticing reward mechanisms remains scant, thus representing a missed opportunity for advancing self-healing strategies. Additionally, the latent potential residing in hydrogen-based prosumers to expedite and elevate the caliber of self-healing processes remains largely untapped, beckoning for further investigation and innovation in this crucial domain. To bridge the above-mentioned gaps, this paper presents a bi-level self-healing strategy for smart grids. It leverages the ADMM algorithm to harness the potential of decentralized smart prosumers, including energy hubs, HRSs, and EVCSs, to facilitate self-healing. Special attention is also given to the role of hydrogen-based facilities in enhancing self-healing within the smart grids. The main contributions of this article include:

- Presenting a bi-level MILP strategy for self-healing planning in smart grids, incorporating smart prosumers and hydrogen-based facilities with a focus on prioritizing load supply. This strategy empowers the SGO to perform self-healing planning, offering options like feeder reconfiguration, implementing LC programs, dispatching MEESs and MFCTs, and utilizing the flexible capacities of smart prosumers.
- Introducing an adaptive ADMM algorithm to enable decentralized coordination between prosumers and SGO while ensuring the security of information sharing. The proposed adaptive version not only attains a globally optimal solution but also significantly enhances solution speed. Through this algorithm, SGO incentivizes prosumers by offering variable rewards for contributing their flexible capacities.
- Unleashing the flexible capacities of smart prosumers to streamline system self-healing and reduce forced load shedding (FLS). In the proposed concept, energy hubs and EVCSs/HRSs have contributed significant capacities to the SGO by implementing an LC program and employing a smart charging strategy, respectively. Furthermore, SGO replenishes its MFCTs with hydrogen from HRSs, deploying them alongside MEES to inject power into critical nodes.
- Incorporating a robust strategy into the proposed bi-level methodology to address uncertainties stemming from stochastic parameters such as load demand and Renewable Energy Sources (RESs) generation. This strategic inclusion bolsters operational reliability and renders the self-healing program adaptable to diverse operational conditions.

2. The Proposed Bi-Level Self-Healing Strategy

The self-healing strategy proposed in this article follows a bi-level structure illustrated in Fig. 1. According to this framework, the first level involves modeling the SGO, while the second level

focuses on modeling smart prosumers, including energy hubs, EVCSs, and HRSs. This concept is designed for managing grid self-healing during emergency situations. Within this framework, grid recovery planning is coordinated between the SGO and smart prosumers. SGO's self-healing options encompass network reconfiguration, dispatching mobile units like MEES and MFCTs, implementing the LC program, and utilizing the flexible capacities of smart prosumers. SGO owns MEES and MFCTs, which are deployed to various grid nodes during emergencies for load recovery. It's noteworthy that SGO conducts self-healing planning using a robust optimization technique, taking into account uncertainties related to RESs generation and load demands.

To facilitate coordination between SGO and smart prosumers, an adaptive ADMM algorithm has been devised, ensuring the attainment of a global optimal solution through an iterative process. In this algorithm, communication between SGO and prosumers occurs in a completely decentralized space, involving the exchange of coupling variables. These coupling variables encompass services exchanged between prosumers and SGO, as well as the associated pricing. In this context, SGO conducts network planning under emergency conditions during each iteration and communicates its requested flexible capacities for grid self-healing, along with the corresponding rewards, to smart prosumers. These prosumers then plan their actions based on the coupling variables received from SGO, update these variables, and return them to SGO. This iterative process ensures that prosumers' planning directly influences the rewards assigned to flexible services. The ADMM algorithm continues iterating until SGO's planning converges with that of smart prosumers.

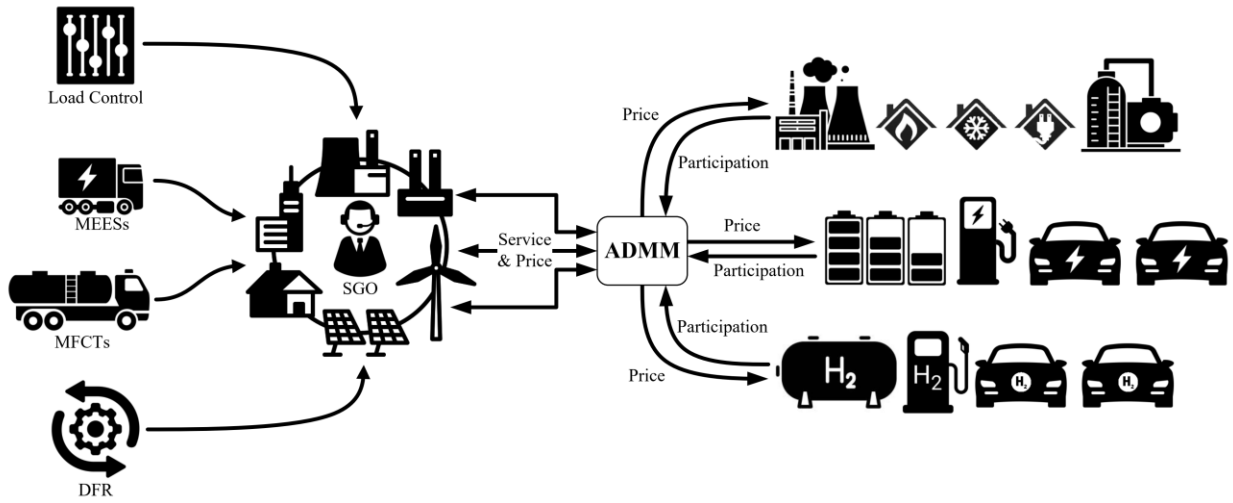

Fig. 1. The architecture of the proposed bi-level self-healing strategy

3. Mathematical Modelling

In this section, a MILP formulation is presented for mathematically modeling the proposed bi-level self-healing strategy. It's important to note that this strategy is designed to manage the self-healing of smart grids in conjunction with multiple smart prosumers during fault occurrence conditions. Furthermore, both SGO and prosumer planning are executed in a fully decentralized manner, with coordination ensured through an adaptive ADMM algorithm.

3.1. First Level (Self-Healing Planning by SGO)

In this subsection, the first stage of the proposed strategy is modeled, where SGO performs network self-healing planning. The objective function for this step is provided in Eq. (1), where SGO aims to minimize the overall cost associated with self-healing. SGO's objective function comprises six components, encompassing costs related to load shedding, network reconfiguration, services procured from prosumers (power and hydrogen), application of LC program, power purchases from the upstream network, and operational expenses for components. π_i^L distinguishes between FLS for non-critical and critical loads. Given that the cost of FLS for critical loads is significantly higher than for non-critical loads, SGO gives priority to supplying power to critical

loads. $P_i^{L,\max}$ represents the requested load (main load) of each node, while $P_{i,t}^{L}$ represents the load supplied in that node. π_{ij}^{F} is the switching cost, considering it in the objective function makes SGO reach the optimal solution with the least switching. $\alpha_{ij,t}^{F}$ indicates the active or inactive status of lines equipped with switches. $P_{h,t}^{Em,Hub}, P_{p,t}^{Em,EVP}, P_{s,t}^{Em,HRS}$ represents the capacity purchased from prosumers, and $\lambda_{h,t}^{E}, \lambda_{p,t}^{E}, \lambda_{s,t}^{E}$ represents the fee paid for each kilowatt. The sixth component of the objective function allocates operational costs to gas turbines, storage systems, MEES, and MFCTs.

$$
\begin{aligned}
&\min \sum_{t}\left[\left(\sum_{i\in N^{Bus}\setminus\left\{N^{DLC},N^{Smart}\right\}} \pi_i^{L}\left(P_i^{L,\max}-P_{i,t}^{L}\right)\right)+\left(\sum_{ij\in N^{Line}} \pi_{ij}^{F}\left(\left|\alpha_{ij,t}^{F}-\alpha_{ij,0}^{F}\right|\right)\right)\right] \\
&+\sum_{t}\left[\sum_{h}\left(\lambda_{h,t}^{E}P_{h,t}^{Em,Hub}\right)+\sum_{p}\left(\lambda_{p,t}^{E}P_{p,t}^{Em,EVP}\right)+\sum_{s}\left(\lambda_{s,t}^{H}H_{s,t}^{Em,Sell}\right)\right]\Delta t \\
&+\sum_{t}\sum_{i\in N^{DLC}}\left(P_i^{L,\max}\sum_{b\in N^{Block}}\left(\upsilon_b^{L}C_b^{L}x_{i,t,b}^{LC}\right)\right)+\sum_{t}\left(\pi_t^{UG}P_t^{S}\right)\Delta t+\sum_{t}\left(\sum_{g}\left(\pi_t^{G}G_{g,t}^{GT}\right)+\sum_{e}\left[\pi^{S}\left(P_{e,t}^{Ch,EES}+P_{e,t}^{Dch,EES}\right)\right]\right) \\
&+\sum_{t}\left(\sum_{n}\sum_{c}\left(\pi_n^{Tr}D_{0,c}x_{c,n,t}^{MEES}\right)+\sum_{m}\sum_{c}\left(\pi_m^{Tr}D_{0,c}u_{c,m,t}^{MFCT}\right)\right)
\end{aligned}
\tag{1}
$$

- **Power Flow and Network Reconfiguration**

In the proposed strategy, SGO conducts network planning while taking into account security and power flow constraints. To achieve this, our model incorporates a Distflow program, ensuring the security of operations and power flow. The program is modeled through (a1)-(a13), where (a1) determines the load supply rate ($P_{i,t}^{L}$) in each node by considering $x_{i,t}^{L}$ as the load supply rate and $P_i^{L,\max}$ as the requested load in the node. (a2) calculates the reactive power of each node based on the supplied load level. (a3) imposes limits on the load supply rate. (a4) maintains voltage fluctuations within a safe range. (a5) constrains active ($P_{ij,t}^{F}$) and reactive ($Q_{ij,t}^{F}$) power flows between nodes *i* and *j* to the apparent power ($S_{ij}^{F,\max}$). The presence/absence of lines in operation is determined by binary variable $\alpha_{ij,t}^{F}$. Note that (a5) is represented in linear form in the simulation

using piecewise method. (a6) and (a7) limit active and reactive powers imported from the upstream network. (a8) accounts for transformers in some nodes, determining the voltage between two consecutive buses. Transformer tap changer settings are determined in (a9) by considering tap number ($n_{ij,t}^{Tap}$) and voltage gain factor (R_{ij}) for each tap. (a10) relates the active and reactive powers of each line to the voltage at both ends. This equation applies only to lines without switches. (a11) updates this relationship for lines with switches, modeled linearly using the Big-M technique. Finally, (a12) and (a13) ensure the balance of active and reactive powers considering all sources of production and consumption.

To maintain the grid's radial structure during reconfiguration, (a14) mandates the selection of one end node as the parent node for each line, using auxiliary binary variables $\beta_{ij,t}^{F}$ and $\beta_{ji,t}^{F}$. This rule is also applied to lines with switches via (a15). (a16) stipulates that each node can only receive power from one side, and (a17) prohibits any node from injecting power into the slack node.

In the proposed concept, SGO has the authority to disconnect loads for industrial customers with LC contracts under specific conditions. (a18) and (a19) model the application of LC program. (a18) determines the amount of LC in each node, allowing SGO to select one LC level using binary variable $x_{i,t,k}^{LC}$. (a19) ensures that only one LC level can be chosen in each node.

$$P_{i,t}^{L} = x_{i,t}^{L} P_{i}^{L,\max} \qquad \forall t, i \qquad \text{(a1)}$$

$$Q_{i,t}^{L} = x_{i,t}^{L} Q_{i}^{L,\max} \qquad \forall t, i \qquad \text{(a2)}$$

$$0 \le x_{i,t}^{L} \le 1 \qquad \forall t, i \qquad \text{(a3)}$$

$$V_{i}^{B,\min} \le V_{i,t}^{B} \le V_{i}^{B,\max} \qquad \forall t, i \qquad \text{(a4)}$$

$$\left(P_{ij,t}^{F}\right)^{2} + \left(Q_{ij,t}^{F}\right)^{2} \le \alpha_{ij,t}^{F} \left(S_{ij}^{F,\max}\right)^{2} \qquad \forall t, ij \qquad \text{(a5)}$$

$$0 \le P_{i,t}^{S} \le P_{i}^{S,\max} \qquad \forall t, i \in N^{Sub} \qquad \text{(a6)}$$

$$0 \le Q_{i,t}^{S} \le Q_{i}^{S,\max} \qquad \forall t, i \in N^{Sub} \qquad \text{(a7)}$$

$$V_{j,t}^{B} = aV_{i,t}^{B} \qquad \forall t, ij \in N^{Trans} \qquad \text{(a8)}$$

$$a = 1 + R_{ij}\left(n_{ij,t}^{Tap}\right) \qquad \forall t, ij \in N^{Trans} \qquad \text{(a9)}$$

$$V_{j,t}^{B} = V_{i,t}^{B} - 2\left(r_{ij}P_{ij,t}^{F} + x_{ij}Q_{ij,t}^{F}\right) \qquad \forall t, ij \in N^{Line} \setminus N^{Switch}, (i,j) \in N^{Bus} \qquad \text{(a10)}$$

$$\left|V_{j,t}^{B} - \left[V_{i,t}^{B} - 2\left(r_{ij}P_{ij,t}^{F} + x_{ij}Q_{ij,t}^{F}\right)\right]\right| = \left(1 - \alpha_{l,t}^{F}\right)M \qquad \forall t, i, j, ij \in N^{Switch} \qquad \text{(a11)}$$

$$P_{ji,t}^{F} = P_{i,t}^{L} + \sum_{k}\kappa_{ik}P_{ik,t}^{F} - P_{i,t}^{G} - P_{t}^{S}\Big|_{i=1} + \sum_{h\in\Lambda_i^h}\left(P_{h,t}^{Hub} - P_{h,t}^{Em,Hub}\right) + \sum_{p\in\Lambda_i^p}\left(P_{p,t}^{EVP} - P_{p,t}^{Em,EVP}\right) + \sum_{s\in\Lambda_i^s}P_{s,t}^{HRS} \qquad \forall t, i \qquad \text{(a12)}$$

$$Q_{ji,t}^{F} = Q_{i,t}^{L} + \sum_{k}\kappa_{ik}Q_{ik,t}^{F} - Q_{i,t}^{G} - Q_{t}^{S}\Big|_{i=1} + \sum_{h\in\Lambda_i^h}\varphi_h\left(P_{h,t}^{Hub} - P_{h,t}^{Em,Hub}\right) + \sum_{p\in\Lambda_i^p}\varphi_p\left(P_{p,t}^{EVP} - P_{p,t}^{Em,EVP}\right) + \sum_{s\in\Lambda_i^s}\varphi_s P_{s,t}^{HRS} \qquad \forall t, i \qquad \text{(a13)}$$

$$\beta_{ij,t}^{F} + \beta_{ji,t}^{F} = 1 \qquad \forall t, ij \in N^{Line} \setminus N^{Switch} \qquad \text{(a14)}$$

$$\beta_{ij,t}^{F} + \beta_{ji,t}^{F} = \alpha_{ij,t}^{F} \qquad \forall t, ij \in N^{Switch} \qquad \text{(a15)}$$

$$\sum_{i}\beta_{ij,t}^{F} \le 1 \qquad \forall t, j \qquad \text{(a16)}$$

$$\beta_{ij,t}^{F} = 0 \qquad \forall t, j \in N^{Sub} \qquad \text{(a17)}$$

$$P_{i,t}^{L} = P_{i}^{L,\max} - P_{i}^{L,\max}\sum_{b\in N^{Block}}\left(\upsilon_b^{L}x_{i,t,b}^{LC}\right) \qquad \forall t, i \in N^{DLC} \qquad \text{(a18)}$$

$$\sum_{b}x_{i,t,b}^{LC} \le 1 \qquad \forall t, i \in N^{DLC} \qquad \text{(a19)}$$

- **Distributed Energy Resources**

(a20) to (a24) introduce the generation functions of DERs. In (a20), the generation function of PV systems is presented, considering hourly radiation, efficiency, and capacity. In (b21), the generation function of Wind Farms (WFs) is described. According to this function, the WF output power depends on the wind speed (v_t) and cut-in and cut-out limits; P_g^{Rate} represents the WF capacity, while v_g^r is the wind speed at which the WF's output power reaches its maximum value. The gas turbine's production function is calculated in (a22), taking into account gas consumption and efficiency. Subsequently, (a23) and (a24) limit the active and reactive powers of the gas turbine, respectively. (a25) specifies that the active generation power at node *i* at hour *t* is

determined based on the operating point of the generation units at that node during that hour. Similarly, (a26) provides this relationship for the reactive power of each node. Since gas turbines are assumed to be the only reactive power source in the system, Eq. (a25) does not consider WFs and PV systems.

$$P_{g,t}^{PV} = \eta^{PV} \frac{R_t}{R_{stc}} P_g^{Rate} \qquad \forall t, g \in N^{PV} \qquad \text{(a20)}$$

$$P_{g,t}^{WT} = \begin{cases} 0 & , \quad v_t < v^{ci} \quad or \quad v_t \geq v^{co} \\ P_g^{Rate} \dfrac{v_t - v^r}{v^{ci} - v^r} & , \quad v^{ci} \leq v_t < v_g^r \\ P_g^{Rate} & , \quad v_g^r \leq v_t < v^{co} \end{cases} \qquad \forall t, g \in N^{WT} \qquad \text{(a21)}$$

$$G_{g,t}^{GT} = P_{g,t}^{GT} \eta^{GT} \qquad \forall t, g \in N^{GT} \qquad \text{(a22)}$$

$$P_g^{GT,\min} \leq P_{g,t}^{GT} \leq P_g^{GT,\max} \qquad \forall t, g \in N^{GT} \qquad \text{(a23)}$$

$$Q_g^{GT,\min} \leq Q_{g,t}^{GT} \leq Q_g^{GT,\max} \qquad \forall t, g \in N^{GT} \qquad \text{(a24)}$$

$$P_{i,t}^{G} = \sum_{g \in \Lambda_i^g} P_{g,t}^{GT} + \sum_{g \in \Lambda_i^g} P_{g,t}^{WT} + \sum_{g \in \Lambda_i^g} P_{g,t}^{PV} \qquad \forall t, i \qquad \text{(a25)}$$

$$Q_{i,t}^{G} = \sum_{g \in \Lambda_i^g} Q_{g,t}^{GT} \qquad \forall t, i \qquad \text{(a26)}$$

- **Energy Storage Systems**

The equations presented in (a27)-(a31) model the utilization of various storage systems considered in this paper. These storage systems include Electrical Energy Storage (EES) units located alongside RES, MEES units within the smart grid, and electrical, thermal and cooling energy storage units in energy hubs. In this context, (a27) calculates the current energy level of the tank ($E_{h,t}^{EES/TES/CES}$) by considering its charging, discharging, and remaining energy from the previous hour ($E_{h,t-1}^{EES/TES/CES}$). (a28) and (a29) impose limits on the maximum charging and discharging capacities of the storage system, respectively. To prevent simultaneous charging and discharging, a binary variable $x_{h,t}^{EES/TES/CES}$ has been introduced. (a30) models the limitation of energy storage capacity in

the reservoir, while (a31) sets the energy level of the storage unit at the start and end of operation equal to $E_h^{In,EES/TES/CES}$.

$$E_{h,t}^{EES/TES/CES} = E_{h,t-1}^{EES/TES/CES} + \left(\eta_{ch}^{EES/TES/CES} P_{h,t}^{Ch,EES/TES/CES} - \frac{P_{h,t}^{Dch,EES/TES/CES}}{\eta_{dch}^{EES/TES/CES}} \right) \Delta t \qquad \forall t,h \quad \text{(a27)}$$

$$P_{h,t}^{Ch,EES/TES/CES} \le \alpha_h^{Ch,\max} E_h^{\max,EES/TES/CES} x_{h,t}^{EES/TES/CES} \qquad \forall t,h \quad \text{(a28)}$$

$$P_{h,t}^{Dch,EES/TES/CES} \le \alpha_h^{Dch,\max} E_h^{\max,EES/TES/CES} \left(1 - x_{h,t}^{EES/TES/CES}\right) \qquad \forall t,h \quad \text{(a29)}$$

$$E_h^{\min,EES/TES/CES} \le E_{h,t}^{EES/TES/CES} \le E_h^{\max,EES/TES/CES} \qquad \forall t,h \quad \text{(a30)}$$

$$E_{h,t=0}^{EES/TES/CES} = E_{h,t=24}^{EES/TES/CES} = E_h^{In,EES/TES/CES} \qquad \forall t,h \quad \text{(a31)}$$

- **Travelling and Operation of Mobile Units**

In the proposed concept, SGO utilizes two types of mobile units, MEES and MFCT, dispatching them to specific candidate nodes in the network during emergency situations. These designated nodes are referred to as connection nodes, where the mobile units can establish connections and inject power. It is assumed that MEES units are fully charged and are promptly dispatched to connection nodes in emergencies. Conversely, MFCTs are initially empty and need to be loaded with hydrogen before being sent to connection nodes. These trucks are equipped with a fuel cell, allowing them to convert the loaded hydrogen into electricity using the fuel cell and subsequently inject it into the connection nodes.

In this article, the concept of an equivalent time network (ETN) is employed to model the movement of mobile units [20]. The ETN concept transforms a transportation network into a time-based representation. It replaces spatial distances with travel times between locations, accounting for variables like loading, traffic and speed limits. This approach facilitates more precise transportation system analysis. In this paper, we have developed the ETN model using mobile units' travel times between locations, resulting in a more straightforward approach with fewer binary variables compared to transportation network-based methods.

In (a32)-(a45), the necessary relations for modeling the movement and operation of mobile units are presented. The movement of mobile units is based on the ETN concept. (a32)-(a35) model the movement of MFCTs. (a32) specifies the location of MFCTs at any given time. If the MFCT is in the depot or traveling, $x_{0,m,t}^{MFCT}$ is equal to 1, and if it is at connection nodes, then $x_{r,m,t}^{MFCT}$ is equal to 1. (a33) indicates that under normal conditions (before a fault occurs), MFCTs are in the depot. (a34) defines the change in the location of MFCTs. According to this relation, when the MFCT arrives at a connection node, $u_{r,m,t}^{MFCT}$ is 1, and when it leaves the connection node, $u_{r,m,t}^{MFCV}$ is -1. (a35) models the travel time of MFCTs between origin and destination points, where $T_{q,r}$ represents the travel time between connection points *q* and *r*.

The operational constraints of MFCTs are presented in (a36)-(a41). (a36) restricts the hydrogen loading of MFCTs. $H_{s,m,t}^{In}$ represents the loaded hydrogen. (a37) states that the total quantity of purchased hydrogen should equal the total quantity of sold hydrogen. (a38) calculates the electric power produced by the fuel cell, taking into account hydrogen consumption, its efficiency (η_s^{FC}), and the low heat value of hydrogen (L^{H_2}). In (a39), the maximum power discharge of MFCT is limited. In (a40), the MFCT tanker's hydrogen level is determined by the previous hour's remaining hydrogen ($H_{m,t-1}^{MFCT}$), injected hydrogen ($H_{s,m,t}^{Buy}$), and fuel cell consumption ($H_{c,m,t}^{FC}$). (a41) models the limitations on the hydrogen level inside the MFCT tank.

(a42) and (a43) model the movement of MEESs, while (a44) and (a45) model their operation. (a42) describes that each MEES can only dispatch to one of the connection points. According to (a43), the MEES can only operate if it has already arrived at a connection point. (a44) imposes a limit on the maximum power discharge of MEES. MEES can only discharge power at connection node *s* if the binary variable $x_{t,m,s}^{MESS}$ is equal to 1. Lastly, (a45) restricts the total energy discharged

by MEES to be less than or equal to the total energy stored in it, considering its discharge efficiency (η_m^{Dch}).

$$\sum_r x_{r,m,t}^{MFCT} + x_{0,m,t}^{MFCT} = 1 \qquad \forall m,t \qquad \text{(a32)}$$

$$x_{0,m,t}^{MFCT} = 1 \qquad \forall m,t \in N^{Normal} \qquad \text{(a33)}$$

$$u_{r,m,t}^{MFCT} = x_{r,m,t}^{MFCT} - x_{r,m,t-1}^{MFCT} \qquad \forall r,m,t \qquad \text{(a34)}$$

$$u_{r,m,t}^{MFCT} Ord(t) + u_{q,m,t}^{MFCT} Ord(t) \geq \sum_t \left(T_{q,r} u_{r,m,t}^{MFCT}\right) + \left(u_{r,m,t}^{MFCT} - 1\right)M - \left(u_{q,m,t}^{MFCT} + 1\right)M \qquad \forall r,m,t \qquad \text{(a35)}$$

$$0 \leq H_{s,m,t}^{Buy} \leq x_{s,m,t}^{MFCT} H_m^{In,\max} \qquad \forall s,m,t \qquad \text{(a36)}$$

$$\sum_m H_{s,m,t}^{Buy} = H_{s,t}^{Em,Sell} \qquad \forall s,t \qquad \text{(a37)}$$

$$P_{c,m,t}^{Dch,MFCT} = \frac{H_{c,m,t}^{FC} \eta_s^{FC} L^{H_2}}{3600} \qquad \forall c,m,t \qquad \text{(a38)}$$

$$0 \leq P_{c,t}^{Dch,MFCT} \leq \sum_m \left(x_{c,m,t}^{MFCT} P_m^{FC,\max}\right) \qquad \forall c,m,t \qquad \text{(a39)}$$

$$H_{m,t}^{MFCT} = H_{m,t-1}^{MFCT} + \sum_s H_{s,m,t}^{Buy} - \sum_c H_{c,m,t}^{FC} \qquad \forall m,t \qquad \text{(a40)}$$

$$0 \leq H_{m,t}^{MFCT} \leq H_m^{MFCT,\max} \qquad \forall m,t \qquad \text{(a41)}$$

$$\sum_c x_{c,n,t}^{MEES} = 1 \qquad \forall n,t \in N^{Normal} \qquad \text{(a42)}$$

$$x_{c,n,t}^{MEES} Ord(t) \geq T_{0,c} x_{c,n,t}^{MFCV} \qquad \forall c,n,t \qquad \text{(a43)}$$

$$0 \leq P_{c,n,t}^{Dch,MEES} \leq x_{c,n,t}^{MESS} P_n^{Dch,\max} \qquad \forall c,n,t \qquad \text{(a44)}$$

$$\sum_t \sum_c P_{c,n,t}^{Dch,MEES} \Delta t \leq E_n^{\max} \eta_n^{Dch} \qquad \forall n \qquad \text{(a45)}$$

3.2. Second Level (Smart Prosumers' Planning)

In the second level, smart prosumers, including energy hubs, EVCSs, and HRSs, are individually modeled. Each of these prosumers conducts its planning based on its objective function, operational constraints, and the signals received from the SGO. These signals indicate the flexible capacities needed by the SGO for network self-healing and the associated rewards.

- **Energy Hubs**

In Eq. (2), the objective function for energy hubs is defined, and (b2)-(b34) outline their operational constraints [32]. Figure (2) illustrates the components of energy hubs and the energy flow between them. Each hub connects to the electricity and gas networks at its entrance and provides electrical, cooling, and heating loads at its exit. Within the hubs, boilers and CHP units burn gas, with boilers generating heat and CHP units generating both electricity and heat. Additionally, each hub is equipped with an EHP system that operates in cooling and heating modes. An absorption chiller supplies cooling load and receives the required heat from CHP and boilers. The proposed model assumes that the hub has an internal LC mechanism, allowing it to curtail a portion of its electrical, heating, and cooling loads in exchange for rewards provided to its subscribers. This mechanism significantly enhances the hub's flexibility to offer flexible capacities to the SGO in emergency situations.

Equation (2) demonstrates that the hub's objective is to minimize its operating costs while considering the rewards for providing emergency services to the SGO. The objective function accounts for costs related to power and gas procurement from the network, the utilization of storage systems, and the implementation of the LC mechanism. As can be seen, the rewards of providing flexible services to SGO are subtracted from the operating costs. Here, π_t^G, $\pi_{h,t}^E$, and $\lambda_{h,t}^E$ denote the gas purchase price, electricity purchase price, and the bonus allocated for flexible services, respectively. υ_b^D represents the load curtailed by the LC mechanism, while C_b^D signifies the associated penalty.

$$\begin{aligned}\min OF_h^{Hub} &= \sum_t \left(\pi_t^G G_{h,t}^{Hub}\right) + \sum_t \left(\pi_{h,t}^E P_{h,t}^{Hub}\right)\Delta t + \sum_t \left[\pi^S \left(P_{h,t}^{Ch,EES/TES/CES} + P_{h,t}^{Dch,EES/TES/CES}\right)\right] \\ &+ \sum_t \left(Z_{h,t}^{Load} \sum_{b\in N^{Block}} \left(\upsilon_b^D C_b^D x_{h,t,b}^Z\right)\right) - \sum_t \left(\lambda_{h,t}^E P_{h,t}^{Em,Hub}\right)\Delta t\end{aligned} \tag{2}$$

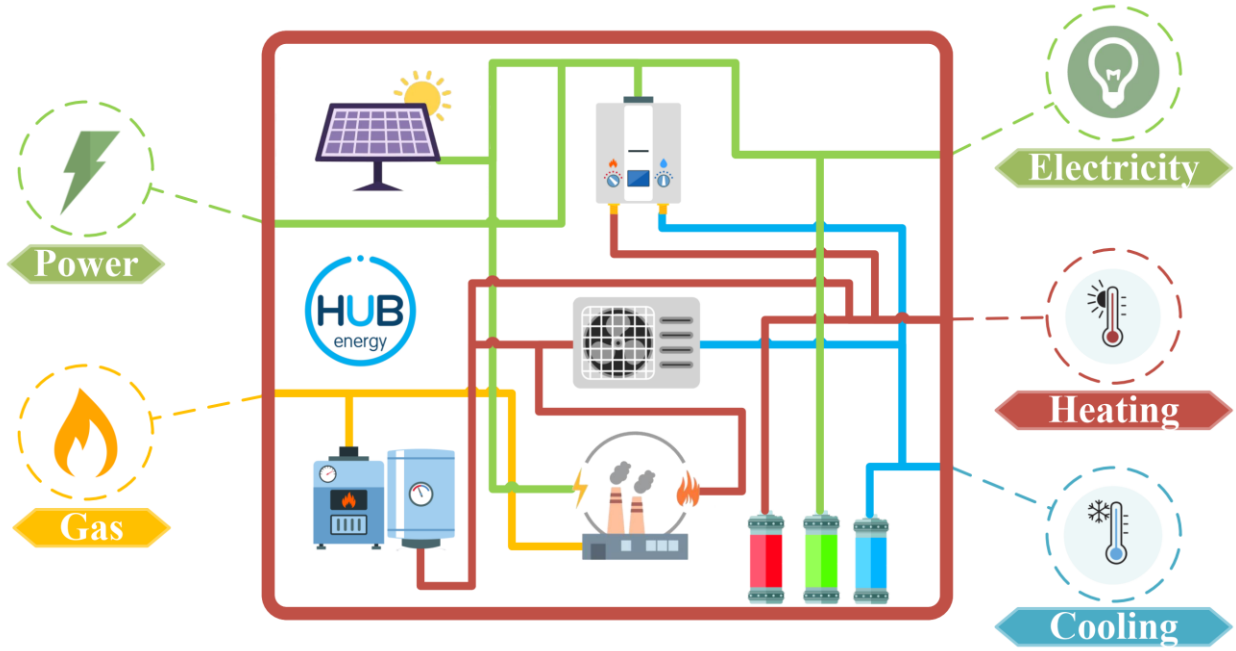

Fig. 2. Configuration of the studied energy hubs

Figure 3 illustrates the permissible operational range of CHP, depicting the interdependence between electricity and heat production. To regulate the operating point of CHP, (b1) imposes a constraint below the line *AB*. Further constraints, (b2) and (b3), bound the CHP's operating point by lines *BC* and *CD*, respectively. Additional limitations on heat and power generation are set by (b4) and (b5), respectively. The gas consumption for CHP is determined by a non-linear function presented in (b6), which involves quadratic terms. These quadratic terms are linearized using a piecewise linear method. Furthermore, to linearize the nonlinear term $P_{h,t}^{CHP} H_{h,t}^{CHP}$, the theory outlined in (b87)-(b14) is employed. This theory proposes discretizing a continuous variable into *N* fixed steps. In (b7), we introduce $PH_{h,t}^{CHP}$ to represent the non-linear term $P_{h,t}^{CHP} H_{h,t}^{CHP}$. (b8) discretizes variable $P_{h,t}^{CHP}$, with P_h^C denoting the CHP's minimum electricity generation rate, and s_h^{CHP} representing the fixed step size. Binary variable $\alpha_{h,t,n}^{CHP}$ determines the presence or absence of discrete gaps in CHP power generation. To determine the size of each step, (b9) considers the

maximum and minimum values of $P_{h,t}^{CHP}$ along with the total number of linearization steps (*N*). Introducing variable $H_{h,t}^{CHP}$ on both sides of Eqs. (b8)-(b10) results in the emergence of a new bilinear term $\alpha_{h,t,n}^{CHP} H_{h,t}^{CHP}$, which is further linearized through the introduction of variable $W_{h,t,n}^{CHP}$ in (b11). Subsequently, (b12) and (b13) present a pair of disjunctive linear inequalities for the linearization of the bilinear term $\alpha_{h,t,n}^{CHP} H_{h,t}^{CHP}$. Finally, (b14) presents the linearized form of (b7) using these introduced variables.

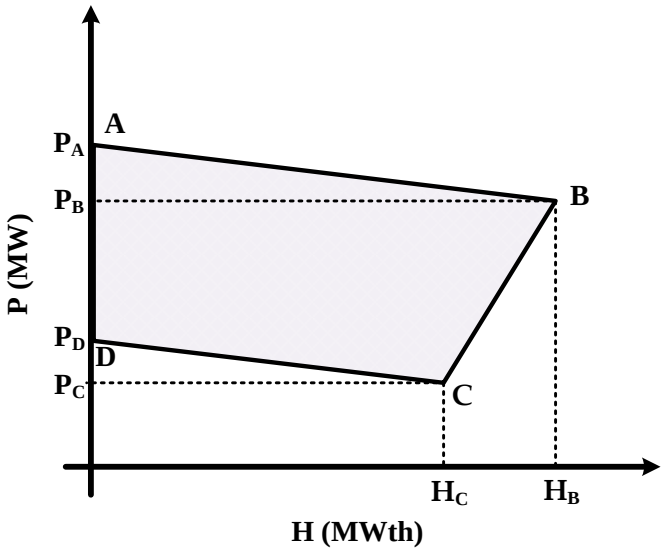

Fig. 3. Feasible operating region of CHP

$$P_{h,t}^{CHP} - P_h^A - \frac{P_h^A - P_h^B}{H_h^A - H_h^B}(H_{h,t}^{CHP} - H_h^A) \le 0 \qquad \forall t,h \qquad \text{(b1)}$$

$$P_{h,t}^{CHP} - P_h^B - \frac{P_h^B - P_h^C}{H_h^B - H_h^C}(H_{h,t}^{CHP} - H_h^B) \ge -(1 - x_{h,t}^{CHP})M \qquad \forall t,h \qquad \text{(b2)}$$

$$P_{h,t}^{CHP} - P_h^C - \frac{P_h^C - P_h^D}{H_h^C - H_h^D}(H_{h,t}^{CHP} - H_h^C) \ge -(1 - x_{h,t}^{CHP})M \qquad \forall t,h \qquad \text{(b3)}$$

$$0 \le H_{h,t}^{CHP} \le H_h^B x_{h,t}^{CHP} \qquad \forall t,h \qquad \text{(b4)}$$

$$P_h^C I_{h,t}^{CHP} \le P_{h,t}^{CHP} \le P_h^A x_{h,t}^{CHP} \qquad \forall t,h \qquad \text{(b5)}$$

$$G_{h,t}^{CHP} = a_h^{CHP} \left(P_{h,t}^{CHP}\right)^2 + b_h^{CHP} P_{h,t}^{CHP} + c_h^{CHP} \left(H_{h,t}^{CHP}\right)^2 + d_h^{CHP} H_{h,t}^{CHP} + e_h^{CHP} P_{h,t}^{CHP} H_{h,t}^{CHP} \qquad \forall t,h \qquad \text{(b6)}$$

$$PH_{h,t}^{CHP} \triangleq P_{h,t}^{CHP} H_{h,t}^{CHP} \qquad \forall t,h \qquad \text{(b7)}$$

$$P_{h,t}^{CHP} = P_h^C + s_h^{CHP} \sum_n \alpha_{h,t,n}^{CHP} \quad \forall t,h \quad \text{(b8)}$$

$$s_h^{CHP} = \frac{\left(P_h^A - P_h^C\right)}{N} \quad \forall t,h \quad \text{(b9)}$$

$$PH_{h,t}^{CHP} \triangleq P_h^C H_{h,t}^{CHP} + s_h^{CHP} \sum_n \left(\alpha_{h,t,n}^{CHP} H_{h,t}^{CHP}\right) \quad \forall t,h \quad \text{(b10)}$$

$$W_{h,t,n}^{CHP} \triangleq \alpha_{h,t,n}^{CHP} H_{h,t}^{CHP} \quad \forall t,h \quad \text{(b11)}$$

$$-\alpha_{h,n}^{CHP} M \le W_{h,t,n}^{CHP} \le \alpha_{h,n}^{CHP} M \quad \forall t,h \quad \text{(b12)}$$

$$H_{h,t}^{CHP} - \left(1-\alpha_{h,t,n}^{CHP}\right) M \le W_{h,t,n}^{CHP} \le H_{h,t}^{CHP} + \left(1-\alpha_{h,t,n}^{CHP}\right) M \quad \forall t,h \quad \text{(b13)}$$

$$PH_{h,t}^{CHP} = P_h^C H_{h,t}^{CHP} + s_h^{CHP} \sum_n W_{h,t,n}^{CHP} \quad \forall t,h \quad \text{(b14)}$$

Boiler operation is governed by (b15) and (b16). In (b15), the heat generated by the boiler ($H_{h,t}^{Boiler}$) is determined based on gas consumption ($G_{h,t}^{Boiler}$) and the efficiency of this asset (η_{gh}^{Boiler}). (b16) also restricts the heat production of the boiler to its capacity. Equations (b17) to (b20) outline the utilization of EHP. In (b17), the electric power consumed by EHP is calculated based on the generation of cooling and heating energy. Here, η_{eh}^{EHP} and η_{ec}^{EHP} denote the conversion efficiency of electrical energy into heating and cooling energy, respectively. (b18) limits the EHP capacity according to the consumed electric power. To account for the inability to simultaneously produce heating and cooling energy, we employ (b19) and (b20). The binary variable $x_{h,t}^{EHP}$ in these equations signifies the operational mode of EHP. AC operation adheres to (b21) and (b22). (b21) calculates the cooling generated by AC based on its heat consumption and asset efficiency, while (b22) restricts the cooling output of AC to its capacity. The modeling of PV systems, electrical, cooling, and thermal storage systems in the hub follows the same principles as those presented for the smart grid.

$$H_{h,t}^{Boiler} = \eta_{gh}^{Boiler} G_{h,t}^{Boiler} \quad \forall t,h \quad \text{(b15)}$$

$$H_{h,t}^{Boiler} \le H_h^{Boiler,\max} \quad \forall t,h \quad \text{(b16)}$$

$$P_{h,t}^{EHP} = \frac{H_{h,t}^{EHP}}{\eta_{eh}^{EHP}} + \frac{C_{h,t}^{EHP}}{\eta_{ec}^{EHP}} \qquad \forall t,h \quad \text{(b17)}$$

$$P_{h,t}^{EHP} \le P_{h}^{EHP,\max} \qquad \forall t,h \quad \text{(b18)}$$

$$H_{h,t}^{EHP} \le x_{h,t}^{EHP} M \qquad \forall t,h \quad \text{(b19)}$$

$$C_{h,t}^{EHP} \le \left(1 - x_{h,t}^{EHP}\right) M \qquad \forall t,h \quad \text{(b20)}$$

$$C_{h,t}^{AC} = \eta_{hc}^{AC} H_{h,t}^{AC} \qquad \forall t,h \quad \text{(b21)}$$

$$C_{h,t}^{AC} \le C_{h,t}^{AC,\max} \qquad \forall t,h \quad \text{(b22)}$$

In the proposed concept, each hub can curtail a portion of its electrical, cooling, and heating loads through the implementation of a LC mechanism. (b23) and (b24) delineate the functioning of this mechanism [33]. (b23) determines the level of electrical, thermal and cooling load demand of the hub after the LC mechanism is executed. $Z_{h,t}^{Load}$ represents the electrical, thermal and cooling load demand of the hub before the LC program is enacted, and υ_b^D specifies the cutoff level. This parameter comprises five levels: 20%, 40%, 60%, 80%, and 100%, with the hub operator selecting one using the binary variable υ_b^D. (b24) stipulates that the hub operator can opt for only one load shedding level at any given time.

Lastly, to maintain the equilibrium of electrical, thermal, cooling, and gas loads within the hub, (b25) to (b28) come into play. (b25) ensures the balance between the hub's electrical power generation and consumption, while (b26) and (b27) guarantee equilibrium in cooling and heating power, respectively. (b28) also asserts that the sum of gas consumed by the boiler and CHP at time *t* must match the gas purchased for that hour.

$$Z_{h,t}^{D} = Z_{h,t}^{Load} - Z_{h,t}^{Load} \sum_{b \in N^{Block}} \left(\upsilon_b^D x_{h,t,b}^{Z}\right) \qquad \forall t,h,z \in \{P,H,C\} \quad \text{(b23)}$$

$$\sum_{b \in N^{Block}} x_{h,t,b}^{Z} \le 1 \qquad \forall t,h,z \in \{P,H,C\} \quad \text{(b24)}$$

$$P_{h,t}^{Hub} + \sum_{g \in \Lambda_h^g} P_{g,t}^{PV} + P_{h,t}^{G} + P_{h,t}^{CHP} + P_{h,t}^{Dch,EES} = P_{h,t}^{D} + P_{h,t}^{EHP} + P_{h,t}^{Ch,EES} + P_{h,t}^{Em,Hub} \qquad \forall t,h \quad \text{(b25)}$$

$$H_{h,t}^{CHP} + H_{h,t}^{Boiler} + H_{h,t}^{EHP} + P_{h,t}^{Dch,TES} = H_{h,t}^{D} + H_{h,t}^{AC} + P_{h,t}^{Ch,TES} \quad \forall t,h \quad \text{(b26)}$$

$$C_{h,t}^{AC} + C_{h,t}^{EHP} + P_{h,t}^{Dch,CES} = C_{h,t}^{D} + P_{h,t}^{Ch,CES} \quad \forall t,h \quad \text{(b27)}$$

$$G_{h}^{Hub} = G_{h,t}^{Boiler} + G_{h,t}^{CHP} \quad \forall t,h \quad \text{(b28)}$$

- **Electric Vehicle Charging Stations**

EVCSs, another category of smart prosumers considered in the proposed concept, have their objective function outlined in (3), and their operational constraints detailed in (c1)-(c5) [32]. These prosumers are equipped with fast-charging infrastructure, PV systems, and EES units. It should be stated that EVCSs possess the capability for Vehicle-to-Grid (V2G) services, meaning they can not only engage in smart charging but also discharge EV batteries in emergency scenarios. As articulated in (3), the objective function for each EVCS revolves around minimizing daily costs minus the rewards received for providing flexible capacities to the SGO. $P_{p,t}^{EVP}$ signifies the power procured from the network, while $\pi_{p,t}^{E}$ represents the price per kilowatt. $P_{h,t}^{Em,EVP}$ and $\lambda_{h,t}^{E}$, respectively, denote the capacities furnished to the SGO and the associated prices.

Equation (c1) stipulates that each EV must be charged equal to or exceeding its predetermined target value ($E_{v,t=T_v^{Dp}}^{EV,Target}$) at the time of departure. Here, $E_{v,t=T_v^{Ar}}^{EV,Ar}$ stands for the energy available in the battery of EVs upon entering the stations. To account for the uncertainty regarding the charging level of the vehicles, $E_{v,t=T_v^{Ar}}^{EV,Ar}$ is generated using a uniform distribution function for each EV, ranging between 40% and 60% of the battery capacity. $P_{v,t}^{Ch,EV}$ and $P_{v,t}^{Dch,EV}$ represent the charged and discharged capacities into/from the EV battery, respectively. Meanwhile, (c2) and (c3) formulate limits for EV battery charging and discharging, introducing the binary variable $x_{v,t}^{EV}$ to prevent concurrent charging and discharging of the EV battery. (c4) models the constraint related to the capacity of EV batteries, and finally, (c5) presents the power balance for EVCSs. In an effort to

safeguard EV battery health, EVCSs only permit EV battery discharge during emergency situations. However, they cannot discharge the batteries of all EVs, as they must consider the energy level constraint of EVs upon leaving the station (c1).

$$\min OF_p^{EVP} = \sum_t \left(\pi_{p,t}^E P_{p,t}^{EVP}\right)\Delta t + \sum_t \left[\pi^S \left(P_{p,t}^{Ch,EES} + P_{p,t}^{Dch,EES}\right)\right] - \sum_t \left(\lambda_{p,t}^E P_{p,t}^{Em,EVP}\right)\Delta t \quad (3)$$

$$E_{v,t=T_v^{Ar}}^{EV,Ar} + \sum_{t=T_v^{Ar}+1}^{T_v^{Dp}} \left(P_{v,t}^{Ch,EV}\eta^{Ch} - \frac{P_{v,t}^{Dch,EV}}{\eta^{Dch}}\right)\Delta t \geq E_v^{EV,Target} \quad \forall v \quad (c1)$$

$$0 \leq P_{v,t}^{Ch,EV} \leq P_{v,t}^{Ch,\max} x_{v,t}^{EV} \quad \forall v,t \quad (c2)$$

$$0 \leq P_{v,t}^{Dch,EV} \leq P_{v,t}^{Dch,\max}\left(1 - x_{v,t}^{EV}\right) \quad \forall v,t \quad (c3)$$

$$E_v^{EV,\min} \leq E_{v,t}^{EV} \leq E_v^{EV,\max} \quad \forall v,t \quad (c4)$$

$$P_{p,t}^{EVP} = \sum_{v\in\Lambda_p^v}\left(P_{v,t}^{Ch,EV} - P_{v,t}^{Dch,EV}\right) - \sum_{g\in\Lambda_p^g} P_{g,t}^{PV} + P_{p,t}^{Ch,EES} - P_{p,t}^{Dch,EES} + P_{h,t}^{Em,EVP} \quad \forall p,t \quad (c5)$$

- **Hydrogen Refueling Stations**

The third category of prosumers incorporated into the proposed concept comprises HRSs, with their objective function delineated in (4) and their operational constraints detailed in (d1)-(d11) [32]. These stations are equipped with PV systems and electrolyzers, primarily serving to charge Fuel Cell Vehicles (FCVs). HRSs produce a portion of the required hydrogen through their electrolyzers and procure the remainder from the market. It is noteworthy that a substantial portion of the necessary power for electrolysis is sourced from the PV systems within the station, with the remainder being acquired through power purchases from the grid. It is assumed that during emergency situations, the SGO will load its MFCTs by procuring hydrogen from HRSs and subsequently dispatch them to connection nodes for power injection into the network.

In accordance with (4), the objective function of HRSs encompasses four parts. The first three parts respectively model the costs incurred from purchasing electricity from the grid, procuring hydrogen from the market, and operating the electrolyzer. The fourth part of this function

encapsulates the rewards garnered from supplying flexible services to the SGO, denoted as hydrogen capacities sold to SGO during emergency situations. (d1) posits that the hydrogen storage level within the station tank ($H_{s,t}^{HRS}$) depends on several factors, including remaining hydrogen from the previous hour ($H_{s,t-1}^{HRS}$), hydrogen generated by the electrolyzer ($H_{s,t}^{El}$), hydrogen purchased from the market ($H_{s,t}^{Buy}$), hydrogen sold to SGO in the form of flexible services ($H_{s,t}^{Em,Sell}$), and injected hydrogen into FCVs ($H_{s,t}^{Load}$). (d2) stipulates that the initial hydrogen storage level within the station at the start of operations equals $H_s^{HRS,In}$. In (d3), the station tank's storage capacity is constrained. (d4) calculates the hydrogen production by the electrolyzer, accounting for efficiency and reaction heat in the electrolysis process (L^{EW}) while considering its electricity consumption ($P_{s,t}^{El}$). (d5) enforces a maximum limit on hydrogen generation by the electrolyzer, aligning with its capacity. (d6) asserts that the hydrogen level in FCV tanks when they depart from the station must meet or exceed a predefined threshold ($E_v^{FCV,Target}$). (d7) models the constraint on hydrogen injection into FCVs per hour, with a corresponding restriction on FCV hydrogen tank capacity delineated in (d8). (d9) specifies that the HRS's load per hour equates to the sum of hydrogen injected into FCVs and hydrogen sold to SGO (in the form of flexible services). Lastly, (d10) asserts that the total power acquired from the grid and derived from PV system must equal the power consumed by the electrolyzer.

$$\min OF_s^{HRS} = \sum_t \left(\pi_{s,t}^E P_{s,t}^{HRS}\right)\Delta t + \sum_t \left(\pi_t^H H_{s,t}^{Buy}\right)\Delta t + \sum_t \left(C_s^{El} P_{s,t}^{El}\right) - \sum_t \left(\lambda_{s,t}^H H_{s,t}^{Em,Sell}\right)\Delta t \tag{4}$$

$$H_{s,t}^{HRS} = H_{s,t-1}^{HRS} + H_{s,t}^{El} + H_{s,t}^{Buy} - H_{s,t}^{Em,Sell} - H_{s,t}^{Load} \qquad \forall t,s \tag{d1}$$

$$H_{s,t=0}^{HRS} = H_s^{HRS,In} \qquad \forall s \tag{d2}$$

$$H_s^{HRS,\min} \le H_{s,t}^{HRS} \le H_s^{HRS,\max} \qquad \forall t,s \tag{d3}$$

$$H_{s,t}^{El} = \frac{3600\eta_s^{El} P_{s,t}^{El}\Delta t}{L^{EW}} \qquad \forall t,s \tag{d4}$$

$$0 \le P_{s,t}^{El} \le P_{s}^{El,\max} \qquad \forall t,s \qquad \text{(d5)}$$

$$E_{v,t=T_v^{Ar}}^{FCV,Ar} + \sum_{t=T_v^{Ar}+1}^{T_v^{Dp}} H_{v,t}^{Ch,FCV}\Delta t \ge E_{v}^{FCV,Target} \qquad \forall t,v \qquad \text{(d6)}$$

$$0 \le H_{v,t}^{Ch,FCV} \le H_{v,t}^{Ch,\max} x_{v,t}^{FCV} \qquad \forall t,v \qquad \text{(d7)}$$

$$E_{v}^{FCV,\min} \le E_{v,t}^{FCV} \le E_{v}^{FCV,\max} \qquad \forall t,v \qquad \text{(d8)}$$

$$H_{s,t}^{Load} = \sum_{v\in\Lambda_s^v} H_{v,t}^{Ch,FCV} \qquad \forall t,s \qquad \text{(d9)}$$

$$P_{s,t}^{HRS} + \sum_{g\in\Lambda_s^g} P_{g,t}^{PV} = P_{s,t}^{El} \qquad \forall t,s \qquad \text{(d10)}$$

4- Solution Method

Figure 4 illustrates a flowchart outlining the steps for implementing the proposed self-healing strategy. Initially, it's important to note that the proposed bi-level MILP strategy is formulated using GAMS, with the GUROBI solver employed for solving it. As per the flowchart, the first step involves inputting all the necessary parameters into GAMS, followed by the modeling of the first and second layers. The first level addresses the self-healing planning problem for SGO, while the second level models smart prosumers, encompassing energy hubs, EVCSs, and HRSs. Subsequently, to establish a connection between the first and second stages, an adaptive ADMM algorithm is introduced, ensuring coordination between SGO and decentralized prosumers with minimal information sharing.

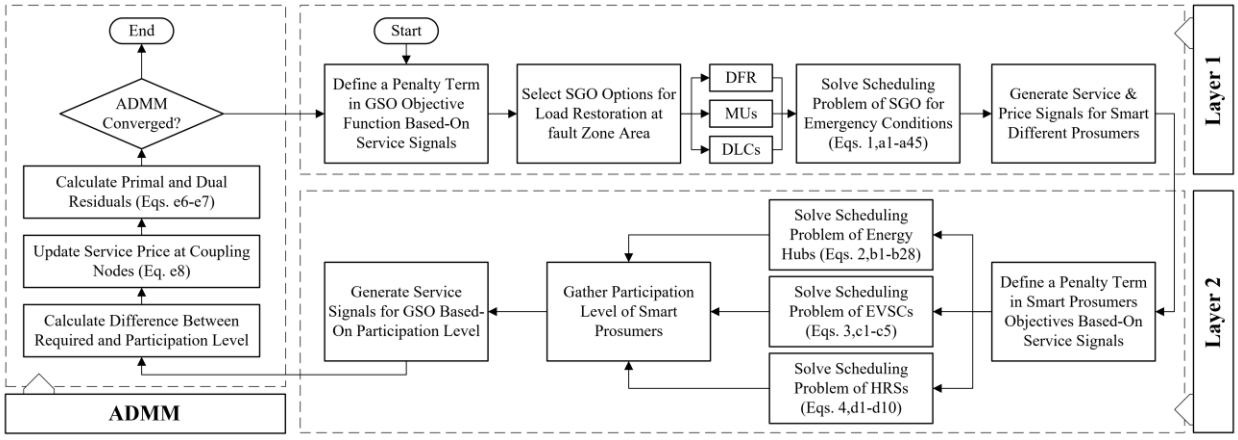

Fig. 4. Flowchart of the proposed bi-level self-healing strategy

4-1- Proposed Adaptive ADMM Algorithm

The ADMM method presents a specialized approach for optimizing problems involving interconnected or linked variables. Its notable advantage lies in its capacity to effectively manage situations where a specific set of variables mutually influence one another. This strategy decomposes complex problems into simpler subproblems, each associated with a specific set of variables. Subsequently, it coordinates the adjustment of these variables by factoring in their connections through a coupling factor. ADMM is unique technique in handling linked variables has demonstrated remarkable efficacy in tackling complex optimization challenges across diverse domains, rendering it a valuable tool in contemporary computational resources. Moreover, ADMM serves as an effective solution for coordinating system operators and decentralized prosumers in self-healing energy networks during emergencies. This method fosters real-time cooperation between system operators and prosumers, enhancing energy distribution, load management, and network restoration while acknowledging their interconnected nature.

ADMM's application in emergency scenarios ensures swift and effective grid recovery, vital for maintaining stability and resilience during crises like natural disasters or equipment failures. By harnessing ADMM's capabilities, system operators and prosumers work seamlessly together, enhancing network self-healing capabilities when they are needed most. This cooperative approach, driven by ADMM, is a significant advancement in ensuring the reliability of energy grids during challenging times.

In the proposed ADMM algorithm, each smart prosumer conducts its programming independently and solely exchanges coupling variables with SGO. These coupling variables encompass the power/hydrogen exchanged between prosumers and SGO, along with their corresponding prices. In the initial iteration of this algorithm, SGO plans its service area (during emergency situations),

subsequently determining the required flexible capacities to manage network self-healing and their corresponding rewards. During this iteration, SGO formulates its planning by considering switching, applying the LC program, and dispatching MEES and MFCTs. Following this, SGO announces these capacities and their associated rewards to the smart prosumers. In the subsequent iteration of the ADMM algorithm, smart prosumers conduct their planning based on SGO's requested capacities and subsequently communicate their participation in these services to SGO. During the third iteration, SGO re-plans its DERs, reconfigures the network, applies the LC program, and dispatches MEES and MFCTs in accordance with the services offered by smart prosumers. SGO updates its required capacities and rewards related to them and communicates these changes to smart prosumers. This iterative process continues until convergence is achieved between prosumers and SGO's programming. Notably, the hourly tariffs related to the purchase of electricity from the grid and hydrogen from the market are considered as input parameters, while the reward paid to prosumers for providing flexible capacities in emergency situations is variable and determined post-convergence of the proposed adaptive ADMM algorithm.

(e1)-(e8) define the mathematical relations essential for implementing the proposed adaptive ADMM algorithm [34]. In (e1)-(e4), the objective functions of SGO, energy hub, EVCS, and HRS are redefined, incorporating a penalty term associated with the ADMM algorithm. This penalty within the objective functions serves to drive convergence in the planning of various actors. ρ^{it} represents the penalty coefficient, which is updated by SGO in each iteration of the ADMM algorithm based on the function presented in (e5). r_p^{it} and r_d^{it} denote primal residuals and dual residuals, respectively, and their values are calculated in accordance with the coupling variable values in (e6) and (e7). Finally, (e8), in each iteration of the ADMM algorithm, computes the reward allocated to flexible services based on the coupling variables. Note that parameters without

a hat refer to SGO's requested capacities, while parameters with a hat denote the capacities provided by prosumers.

$$\begin{cases} Penalty_{h,it}^{Hub} = \dfrac{\rho^{it}}{2}\left\|\widehat{P}_{h,t,it}^{Em,Hub} - P_{h,t,it}^{Em,Hub}\right\|_2^2 \\ Penalty_{p,it}^{EVP} = \dfrac{\rho^{it}}{2}\left\|\widehat{P}_{p,t,it}^{Em,EVP} - P_{p,t,it}^{Em,EVP}\right\|_2^2 \\ Penalty_{s,it}^{HRS} = \dfrac{\rho^{it}}{2}\left\|\widehat{H}_{s,t,it}^{Em,Sell} - H_{s,t,it}^{Em,Sell}\right\|_2^2 \end{cases} \quad \text{(e1)}$$

$$\begin{aligned} \min OF_{h,it}^{Hub} &= \sum_t \left(\pi_t^G G_{h,t}^{Hub}\right) + \sum_t \left(\pi_{h,t}^E P_{h,t}^{Hub}\right)\Delta t + \sum_t \left[\pi^S \left(P_{h,t}^{Ch,EES/TES/CES} + P_{h,t}^{Dch,EES/TES/CES}\right)\right] \\ &+ \sum_t \left(Z_{h,t}^{Load} \sum_{b\in N^{Block}} \left(\upsilon_b^D C_b^D x_{h,t,b}^Z\right)\right) - \sum_t \left(\lambda_{h,t}^E P_{h,t}^{Em,Hub}\right)\Delta t + \sum_t \left(\frac{\rho^{it}}{2}\left\|\widehat{P}_{h,t,it}^{Em,Hub} - P_{h,t,it}^{Em,Hub}\right\|_2^2\right) \end{aligned} \quad \text{(e2)}$$

$$\begin{aligned} \min OF_{p,it}^{EVP} &= \sum_t \left(\pi_{p,t}^E P_{p,t}^{EVP}\right)\Delta t + \sum_t \left[\pi^S \left(P_{p,t}^{Ch,EES} + P_{p,t}^{Dch,EES}\right)\right] - \sum_t \left(\lambda_{p,t}^E P_{p,t}^{Em,EVP}\right)\Delta t \\ &+ \sum_t \left(\frac{\rho^{it}}{2}\left\|\widehat{P}_{p,t,it}^{Em,EVP} - P_{p,t,it}^{Em,EVP}\right\|_2^2\right) \end{aligned} \quad \text{(e3)}$$

$$\begin{aligned} \min OF_{s,it}^{HRS} &= \sum_t \left(\pi_{s,t}^E P_{s,t}^{HRS}\right)\Delta t + \sum_t \left(\pi_t^H H_{s,t}^{Buy}\right)\Delta t + \sum_t \left(C_s^{El} P_{s,t}^{El}\right) - \sum_t \left(\lambda_{s,t}^H H_{s,t}^{Em,Sell}\right)\Delta t \\ &+ \sum_t \left(\frac{\rho^{it}}{2}\left\|\widehat{H}_{s,t,it}^{Em,Sell} - H_{s,t,it}^{Em,Sell}\right\|_2^2\right) \end{aligned} \quad \text{(e4)}$$

$$\rho^{it+1} = \begin{cases} \sigma^{incr}\rho^{it} & , \ \left\|r^{it}\right\|_2 > \left\|d^{it}\right\|_2 \\ \dfrac{\rho^{it}}{\sigma^{decr}} & , \ \left\|d^{it}\right\|_2 >> \left\|r^{it}\right\|_2 \\ \rho^{it} & , \ \text{Otherwise} \end{cases} \quad \text{(e5)}$$

$$r_p^{it} = \sum_h \sum_t \left(\left\|\left(P_{h,t,it}^{Em,Hub} - \widehat{P}_{h,t,it}^{Em,Hub}\right)\right\|_2\right) + \sum_p \sum_t \left(\left\|\left(P_{p,t,it}^{Em,EVP} - \widehat{P}_{p,t,it}^{Em,EVP}\right)\right\|_2\right) + \sum_s \sum_t \left(\left\|\left(H_{s,t,it}^{Em,Sell} - \widehat{H}_{s,t,it}^{Em,Sell}\right)\right\|_2\right) \quad \text{(e6)}$$

$$r_d^{it} = \sum_h \sum_t \left(\left\|\left(\lambda_{h,t}^{E,it+1} - \lambda_{h,t}^{E,it}\right)\right\|_2\right) + \sum_p \sum_t \left(\left\|\left(\lambda_{p,t}^{E,it+1} - \lambda_{p,t}^{E,it}\right)\right\|_2\right) + \sum_s \sum_t \left(\left\|\left(\lambda_{s,t}^{H,it+1} - \lambda_{s,t}^{H,it}\right)\right\|_2\right) \quad \text{(e7)}$$

$$\begin{cases} \lambda_{h,t}^{E,it+1} = \max\left(\lambda_{h,t}^{E,it} + \rho^{it}\left(\widehat{P}_{h,t,it}^{Em,Hub} - P_{h,t,it}^{Em,Hub}\right), 0\right) \\ \lambda_{p,t}^{E,it+1} = \max\left(\lambda_{p,t}^{E,it} + \rho^{it}\left(\widehat{P}_{p,t,it}^{Em,EVP} - P_{p,t,it}^{Em,EVP}\right), 0\right) \\ \lambda_{s,t}^{H,it+1} = \max\left(\lambda_{s,t}^{H,it} + \rho^{it}\left(H_{s,t,it}^{Em,Sell} - \widehat{H}_{s,t,it}^{Em,Sell}\right), 0\right) \end{cases} \quad \text{(e8)}$$

4-2- Robust Modelling of Self-Healing Planning

In (e1)-(e10), we introduce the relations for robust self-healing planning by SGO [35]. (e1)-(e3) model fluctuations associated with RESs. In (e1), the acceptable range of RES fluctuations is

determined by considering the predicted output (P_t^{REN}), the maximum deviation value ($P_t^{REN,Deviation}$), and the deviation variable (α_t^{REN}). (e2) ensures that variable α_t^{REN} remains between zero and one. (e3) states that the sum of deviations throughout the planning period should be less than Γ^{REN}. The dual variables q_t^{REN} and λ^{REN} are associated with constraints (e2) and (e3). Moving on to (e4)-(e6), these relations model the upper limits on load fluctuations. In (e7), the active power balance equation introduced in (15) is reformulated to account for uncertainties stemming from RESs and load demand. For robust optimization aiming to maximize α_t^{REN} and α_t^{D}, generation uncertainties are assigned a negative sign, while load uncertainty is given a positive sign in (e7). (e8) and (e9) present dual constraints pertaining to α_t^{REN} and α_t^{D}, respectively. Lastly, in (e10), the active power balance equation presented in (e7) is reconfigured by replacing uncertain components ($\alpha_{i,t}^{L} P_{i,t}^{L,Deviation}$, $\alpha_{g,t}^{WT} P_{g,t}^{WT,Deviation}$ and $\alpha_{g,t}^{PV} P_{g,t}^{PV,Deviation}$) with their dual equivalents.

$$P_t^{REN} \in \left[\tilde{P}_t^{REN} - \alpha_t^{REN} P_t^{REN,Deviation}, \tilde{P}_t^{REN} + \alpha_t^{REN} P_t^{REN,Deviation} \right] \tag{e1}$$

$$0 \le \alpha_t^{REN} \le 1,\ q_t^{REN} \tag{e2}$$

$$\sum_t \alpha_t^{REN} \le \Gamma^{REN},\ \lambda^{REN} \tag{e3}$$

$$P_t^{D} \in \left[\tilde{P}_t^{D} - \alpha_t^{D} P_t^{D,Deviation}, \tilde{P}_t^{D} + \alpha_t^{D} P_t^{D,Deviation} \right] \tag{e4}$$

$$0 \le \alpha_t^{D} \le 1,\ q_t^{D} \tag{e5}$$

$$\sum_t \alpha_t^{D} \le \Gamma^{D},\ \lambda^{D} \tag{e6}$$

$$\begin{aligned} P_{ji,t}^{F} = {} & \tilde{P}_{i,t}^{L} + \alpha_{i,t}^{L} P_{i,t}^{L,Deviation} + \sum_k \kappa_{ik} P_{ik,t}^{F} + \sum_{h \in \Lambda_i^h} \left(P_{h,t}^{Hub} - P_{h,t}^{Em,Hub} \right) + \sum_{p \in \Lambda_i^p} \left(P_{p,t}^{EVP} - P_{p,t}^{Em,EVP} \right) + \sum_{s \in \Lambda_i^s} P_{s,t}^{HRS} \\ & - \left(\sum_{g \in \Lambda_i^g} P_{g,t}^{GT} + \sum_{g \in \Lambda_i^g} \left(\tilde{P}_{g,t}^{WT} - \alpha_{g,t}^{WT} P_{g,t}^{WT,Deviation} \right) + \sum_{g \in \Lambda_i^g} \left(\tilde{P}_{g,t}^{PV} - \alpha_{g,t}^{PV} P_{g,t}^{PV,Deviation} \right) \right) - P_t^{S} \Big|_{i=1} \end{aligned} \tag{e7}$$

$$q_t^{REN} + \lambda^{REN} \ge P_t^{REN,Deviation} \tag{e8}$$

$$q_t^{D} + \lambda^{D} \ge P_t^{D,Deviation} \tag{e9}$$

$$P_{ji,t}^{F}=\tilde{P}_{i,t}^{L}+\lambda_{i}^{L}\Gamma_{i}^{L}+q_{i,t}^{L}+\sum_{k}\kappa_{ik}P_{ik,t}^{F}+\sum_{h\in\Lambda_{i}^{h}}\left(P_{h,t}^{Hub}-P_{h,t}^{Em,Hub}\right)+\sum_{p\in\Lambda_{i}^{p}}\left(P_{p,t}^{EVP}-P_{p,t}^{Em,EVP}\right)+\sum_{s\in\Lambda_{i}^{s}}P_{s,t}^{HRS}$$
$$-\left(\sum_{g\in\Lambda_{i}^{g}}P_{g,t}^{GT}+\sum_{g\in\Lambda_{i}^{g}}\left(\tilde{P}_{g,t}^{WT}-\lambda_{g}^{WT}\Gamma_{g}^{WT}-q_{g,t}^{WT}\right)+\sum_{g\in\Lambda_{i}^{g}}\left(\tilde{P}_{g,t}^{PV}-\lambda_{g}^{PV}\Gamma_{g}^{PV}-q_{g,t}^{PV}\right)\right)-P_{t}^{S}\Big|_{i=1} \quad \text{(e10)}$$

5- Simulation Results

5-1- Input Data

In this section, we analyze the results of implementing the proposed bi-level strategy on a modified IEEE 118-node distribution test system [32]. As per Fig. 5, the network comprises various smart prosumers connected to different nodes, including 20 energy hubs, 11 EVCSs, and 6 HRSs. Two depots, housing the MEES and MFCTs before a fault occurs, are located at nodes 27 and 96. Specifically, SGO has 3 MEESs and 2 MFCTs. The nodes designated as connection points for mobile units are highlighted in green, while nodes with industrial customers under LC contracts are marked in orange. Nodes with non-critical loads are depicted in black, and critical loads are identified in red. Additionally, red dashed lines indicate branches with switches for DFR. Table 1 provides details concerning smart prosumers and mobile units, while Table 2 offers information about network components. Table 2 reveals that approximately 46% of the production capacity stems from PV systems, around 27% is attributed to WFs, and about 27% is derived from gas turbines. Input parameters for simulation are depicted in Figs. 6a-6j. Table 3 outlines the configurations of various study cases designed to assess the effectiveness of the proposed bi-level strategy, considering options such as LC, program mobile units, and the flexible capacities of smart prosumers. In all cases, it is assumed that the branch between nodes 1 and 3 is disconnected from 14:00 to 21:00.

Table 1. Information on smart prosumers and mobile units

Energy Hubs								
Type	Locations	Assets Capacity (kW)						
		CHP	Boiler	AC	PV	EHP	EES	TES	CES
A	7-14-17-21	700	300	250	200	300	250	200	300

	24-40-48 51-56-59								
B	64-66-72 77-87-92	800	400	350	150	150	200	150	200
C	99-101 109-115	700	400	300	200	200	250	200	250

Electric Vehicle Charging Stations					
Type	Locations	EV Capacity (kW)	Number of EVs	PV (kW)	EES (kW)
A	5-16-33-43 57-68-83	40	100	200	100
B	88-95-103-118	40	150	250	150

Hydrogen Refueling Stations				
Type	Locations	FCV Capacity (kg)	Number of FCVs	PV (kW)
A	18-61-45	6	70	400
B	70-79-98	5	90	500

Table 2. Information on smart grid components

Unit No.	Type	Location	Capacity (kW)	Unit No.	Type	Location	Capacity (kW)
1	GT	9	800	10	WT	76	1400
2	GT	34	900	11	PV	3	1500
3	GT	53	850	12	PV	15	1300
4	GT	63	1100	13	PV	39	1400
5	GT	90	1000	14	PV	55	1200
6	GT	112	800	15	PV	69	1300
7	WT	6	1300	16	PV	78	1300
8	WT	36	1600	17	PV	113	1400
9	WT	58	1300	-	-	-	-

Table 3. Configuration of the studied cases.

Case Studies	**DLC**	**Smart Prosumers**			**Mobile Units**	
		Energy Hubs	**EVCSs**	**HRSs**	**MEESs**	**MFCTs**
A1	×	×	×	×	×	×
A2	✓	×	×	×	×	×
B1	✓	✓	×	×	×	×
B2	✓	✓	✓	×	×	×
B3	✓	✓	✓	✓	×	×
C1	✓	✓	✓	✓	✓	×
C2	✓	✓	✓	✓	✓	✓

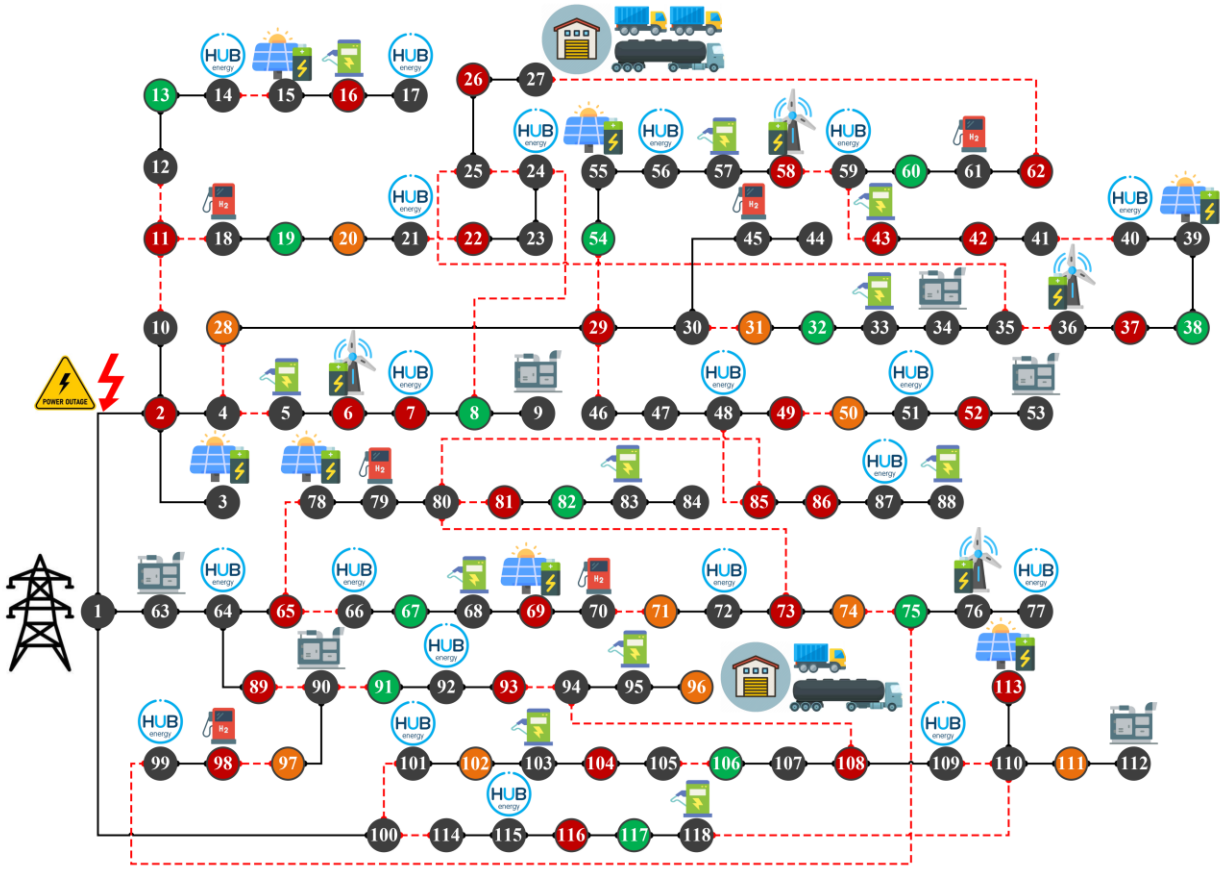

Fig. 5. The structure of modified IEEE 118-node distribution system

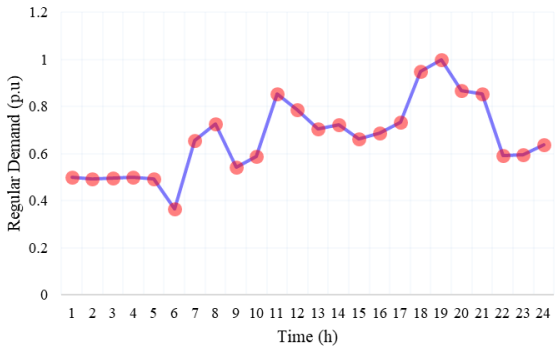

(a) Electricity demand of regular loads

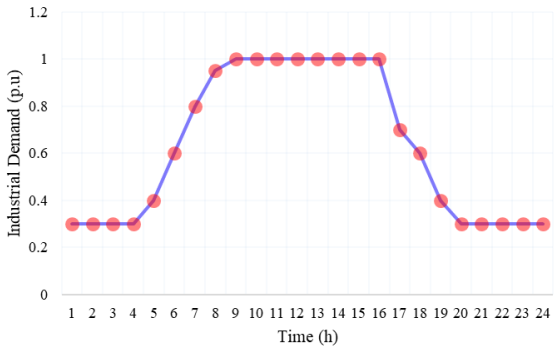

(b) Electricity demand of industrial units

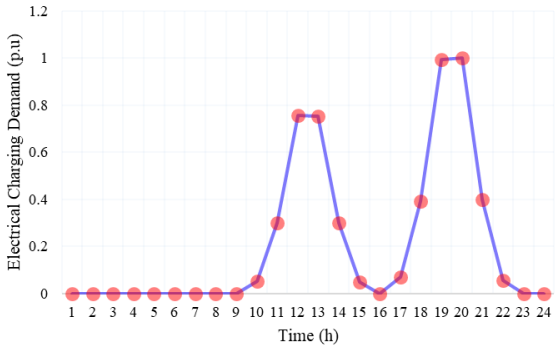

(c) Electricity demand of EVCSs

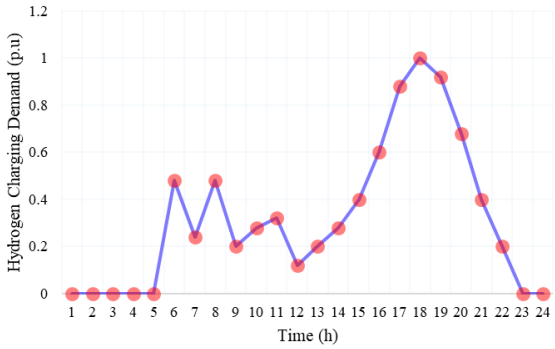

(d) Hydrogen demand of HRSs

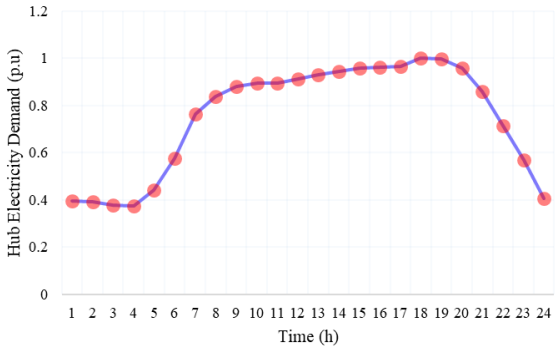

(e) Electricity demand of energy hubs

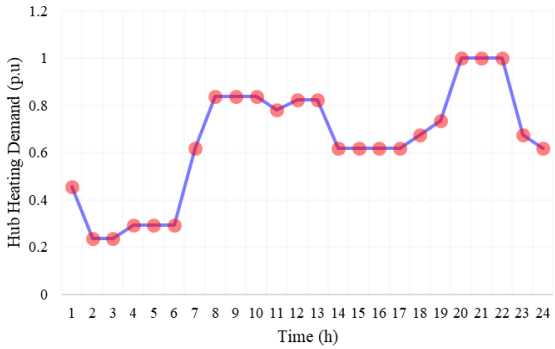

(f) Heating demand of energy hubs

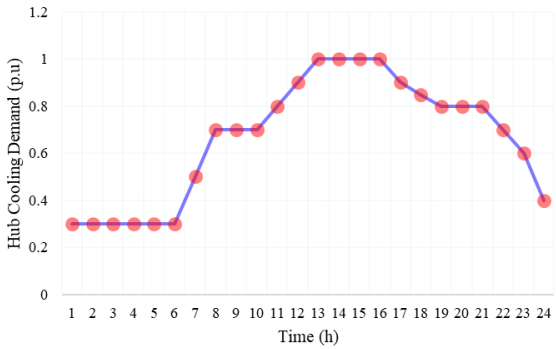

(g) Cooling demand of energy hubs

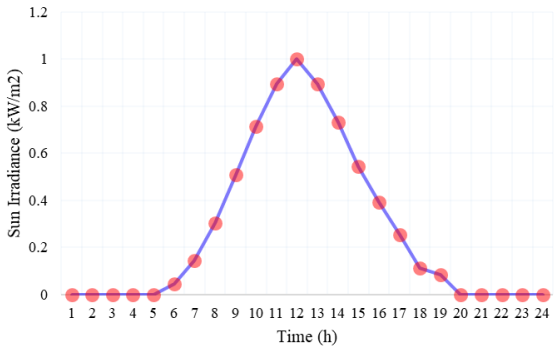

(h) Sun irradiance

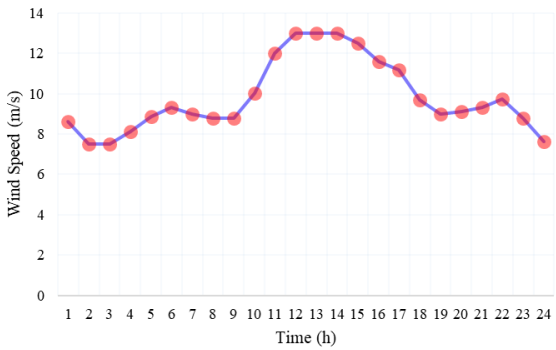

(i) Wind speed

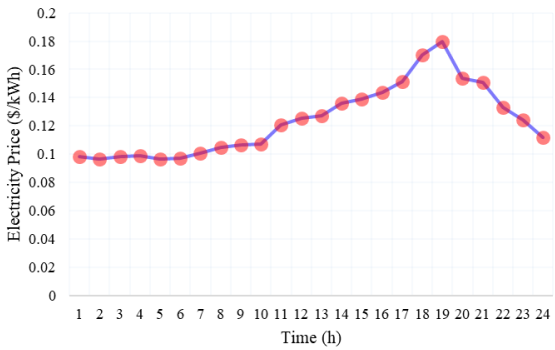

(j) Electricity price

Fig. 6. Input parameters for simulation [32]

5-2- Results of Cases A1 & A2

In Table 4, the results from the simulation of A1 and A2 are presented. Note that the table results are for the emergency period from 14:00 to 21:00. In A1, the only self-healing option available to SGO is DFR, whereas in A2, SGO has the additional option of using LC program along with DFR. The table's results show that the implementation of the LC program in A2 has resulted in a 39.52% reduction in FLS costs, consequently leading to a 27.99% reduction in SGO operating costs during the emergency period. This reduction is primarily attributed to the lower cost of DLC compared to FLS. Figure 7a illustrates the amount of DLC and FLS in each node. In A2, a portion of the loads in nodes 20, 28, 31, and 50 have been curtailed under the LC contract, while FLS has been prevented in node 2, 6, 7, 29, 49 and 52. Figure 7b compares the critical loads provided in A1 and A2. In A2, critical loads in nodes 2, 6, 7, 29, 49 and 52 have been safeguarded from interruption. The resulting DFR topologies in A1 and A2 are depicted in Figs. 8a and 8b, respectively. Figure 8a illustrates that in A1, SGO has established a new path to energize nodes within the fault zone by enabling lines (48-85), (43-59) and (27-62) while disabling lines (1-2), (35-36), and (24-25), all while maintaining the network's radial structure. Figure 8b reveals that in A2, SGO has provided a new path to energize nodes within the fault zone by activating lines (24-25) and (8-24). The change in the power flow path between A1 and A2 is attributed to the simultaneous execution of the DFR and LC program in A2. The availability of both DFR and LC options in A2 has led to a shift in SGO's planning. In A2, SGO has disconnected 8128.79 kWh, 8847.05 kWh, 7639.39 kW and 13665.35 kWh of industrial loads connected to buses 20, 28, 31 and 50, respectively, using the LC program.

Table 4. Results of Case A1 & A2

Case A1							
Entity	Expenses during Event ($)						
	Components	Mobile Units	LC	FLS	Exchange	Reward	Sum

SG	303.2	0	0	223431.18	26551.91	0	250286.29
Energy Hubs	1608.09	-	0	-	-2947	0	-1338.91
EVCSs	39.09	-	0	-	720.92	0	760.01
HRSs	44.28	-	0	-	-233.05	0	-188.77
Case A2							
Entity	Components	Mobile Units	LC	FLS	Exchange	Reward	Sum
SG	303.2	0	18921.35	135110.26	25886.16	0	180220.97
Energy Hubs	1607.61	-	0	-	-2942.97	0	-1335.36
EVCSs	42.3	-	0	-	700.69	0	742.99
HRSs	44.28	-	0	-	-233.05	0	-188.77

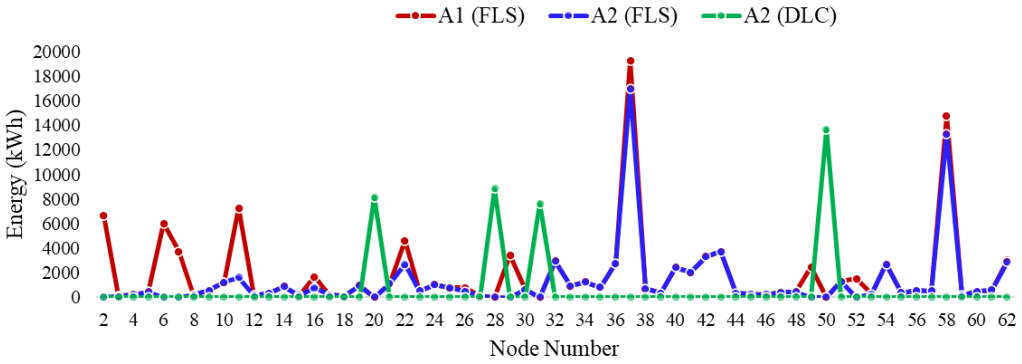

(a) FLS and DLC at each node

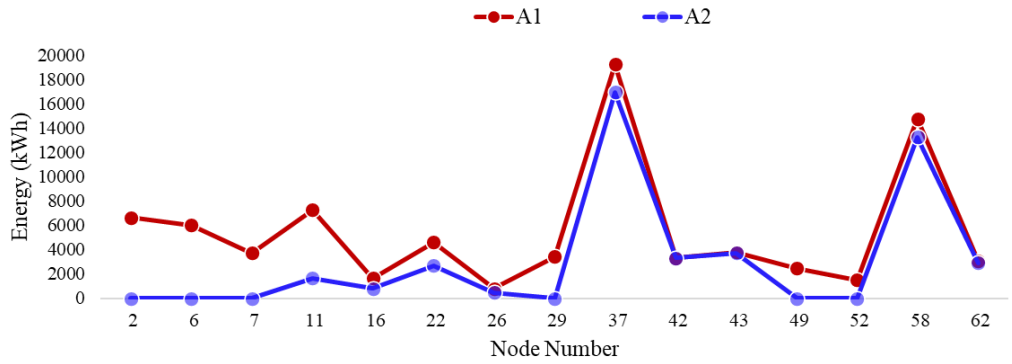

(b) FLS at critical loads

Fig. 7. The rate of FLS in Cases A1 & A2

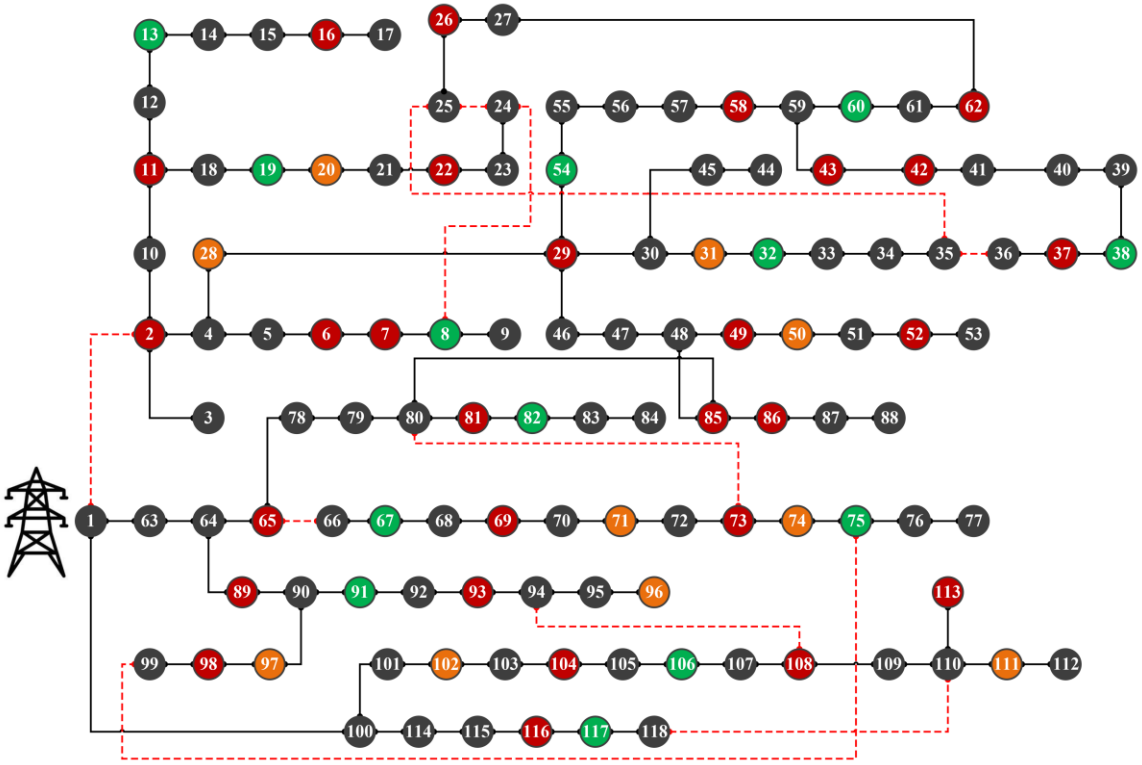

(a) Topology obtained from DFR in A1

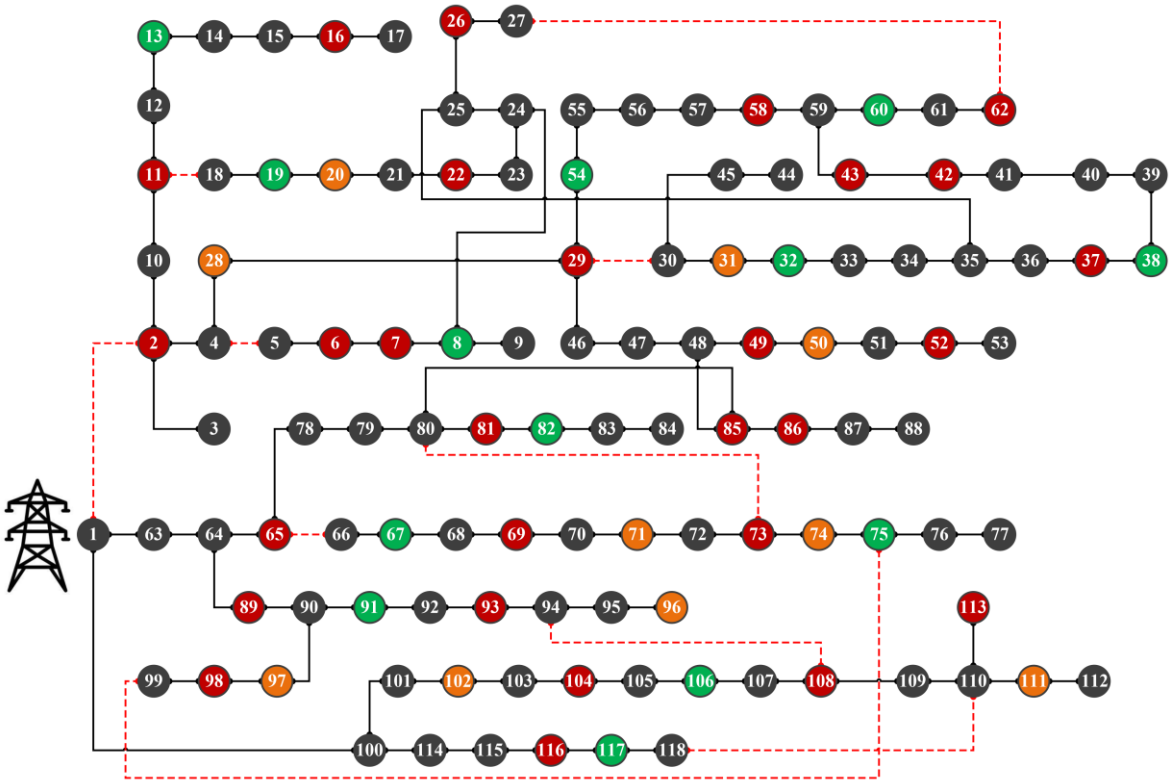

(b) Topology obtained from DFR in A2

Fig. 8. Network topology in Cases A1 and A2

3- Results of Cases B1-B3

In this subsection, we present the results obtained from simulations B1-B3. These simulations involve energy hubs in B1, EVPLs in B2, and HRSs in B3 participating in self-healing planning and providing flexible capacities to SGO. The numerical results from these simulations are summarized in Table 5. According to the results in the table, the involvement of energy hubs in self-healing planning resulted in a 23.92% reduction in FLS costs. In this scenario, SGO acquired 28,318.69 kWh of energy from energy hubs, thereby avoiding a $32,329.63 FLS fine. Furthermore, energy hubs in B1 generated a profit of $10,194.73 by supplying flexible capacities to SGO, reducing their total costs by 12.37% compared to A2. Figure 9a compares the network's FLS levels in B1 and A2, illustrating the capacities provided by energy hubs. It is evident that in B1, the FLS levels have decreased in several nodes compared to A2, thanks to the capacities supplied by the hubs. Figure 9b also compares the supply of critical loads in B1 and A2, showing a higher level of critical load supply in B1. Figures 10a and 10b display the consumption and power exchange profiles of the energy hub connected to node 7 in A2 and B1. Figure 10a indicates that in A2, this hub fully met its electrical, thermal, and cooling load requirements. Conversely, Figure 10b reveals that in B1, this hub activated the LC mechanism, cutting off 60% of its electrical loads and injecting a total of 1,915.44 kWh of energy into the grid during the emergency period (from 14:00 to 21:00). The results from Table 5 demonstrate that in B2, the activation of EVCSs in self-healing planning reduced FLS costs by 2.96% compared to B1. Additionally, the simultaneous involvement of EVCSs and HRSs in B3 resulted in a 1.32% reduction in FLS costs compared to B2 and a 4.25% reduction compared to B1. These numerical findings clearly illustrate that increased participation of smart prosumers in self-healing planning leads to reduced FLS and the associated fines. Figure 11a compares the FLS levels for each node in B1-B3, showing that FLS is reduced in B3 compared

to B2 and B1. This reduction can be attributed to the simultaneous participation of energy hubs, EVCSs, and HRSs in self-healing planning, providing significant capacities to SGO. Figure 11b confirms that in B3, the FLS rate at critical loads is lower than in B2 and B1. Figures 12a and 12b depict the schedules obtained for an EVCS and an HRS in B1 and B3. Figure 12a shows that in B2, when EVCS is activated in self-healing, its consumption curve changed, moving a substantial portion of EV charging from the emergency period to the post-event period. This resulted in EVCS reducing its load by a total of 334.69 kWh during the emergency period and subsequently selling approximately 124.84 kWh of energy to the grid. Figure 12b demonstrates that HRS performed similarly to EVCS in B3, adjusting the charging schedule of FCVs during the emergency period and supplying 30.24 kg of hydrogen to the grid. These results underscore the significant potential of EVCSs and HRSs in assisting the system during emergency situations.

Table 5. Results of Case B2-B3

Case B1							
Entity	Expenses during Event ($)						
	Components	Mobile Units	LC	FLS	Exchange	Reward	Sum
SG	303.2	0	18921.35	135110.26	25886.16	0	180220.97
Energy Hubs	1607.61	-	0	-	-2942.97	0	-1335.36
EVCSs	42.3	-	0	-	700.69	0	742.99
HRSs	44.28	-	0	-	-233.05	0	-188.77
Case B2							
Entity	Components	Mobile Units	LC	FLS	Exchange	Reward	Sum
SG	303.2	0	15457.09	102780.63	29185.52	10194.73	157921.17
Energy Hubs	1612.26	-	7380.98	-	-6534.42	-10194.73	-7735.91
EVCSs	39.9	-	0	-	715.81	0	755.71
HRSs	44.28	-	0	-	-233.05	0	-188.77
Case B3							
Entity	Components	Mobile Units	LC	FLS	Exchange	Reward	Sum
SG	303.2	0	14091.83	99729.06	29855.61	11679.41	155659.11
Energy Hubs	1602.89	-	7550.19	-	-6572.93	-10428.43	-7848.28
EVCSs	39.9	-	871.93	-	374.64	-1250.98	35.49
HRSs	26.14	-	47.75	-	-417.68	-65.32	-409.11

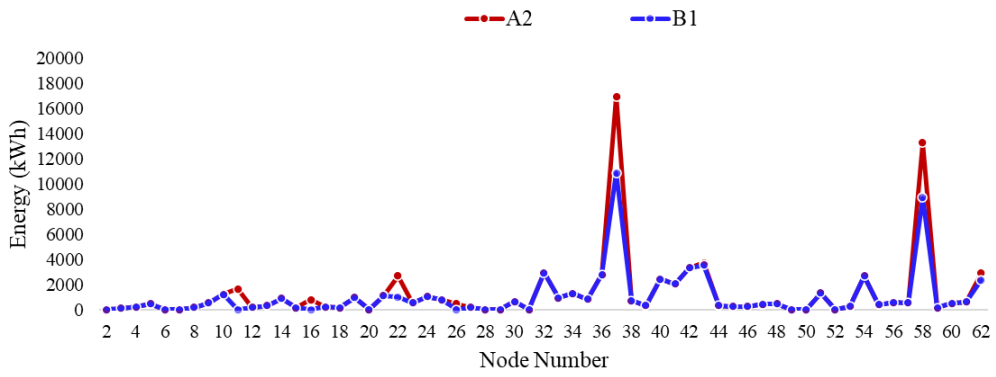

(a) FLS at each node

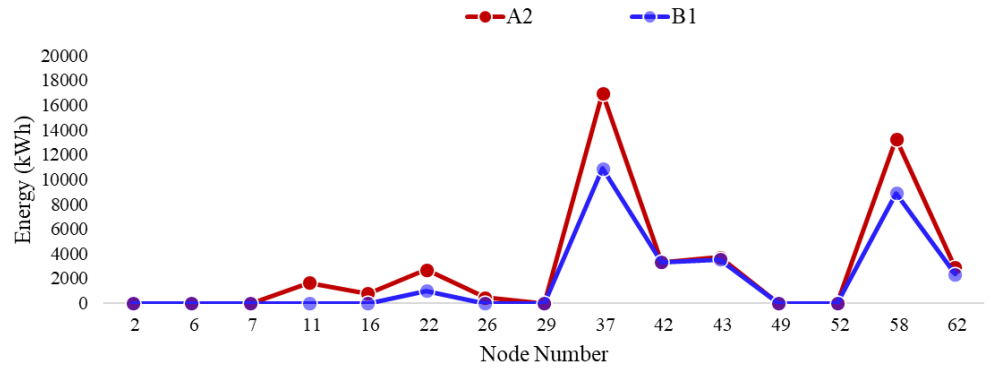

(b) FLS at critical loads

Fig. 9. The rate of FLS in Cases A2 & B1

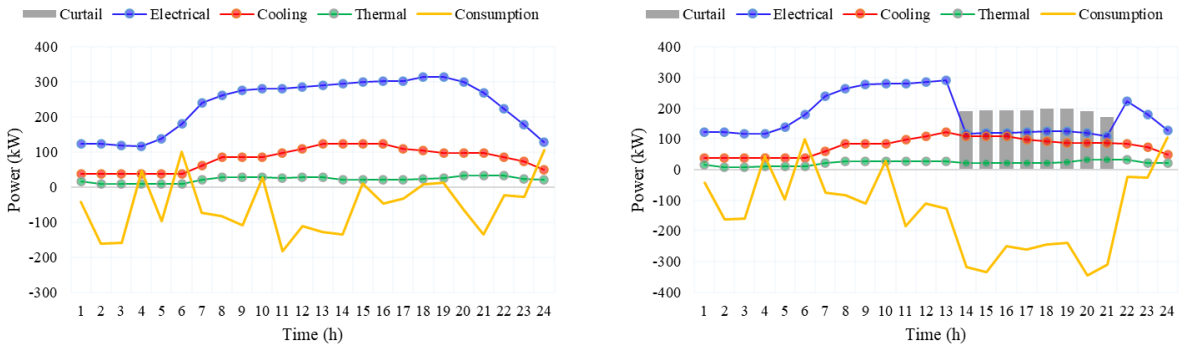

(a) Case A2 (b) Case B1

Fig. 10. The consumption rate and power exchange of an energy hub in Cases A2 and B1

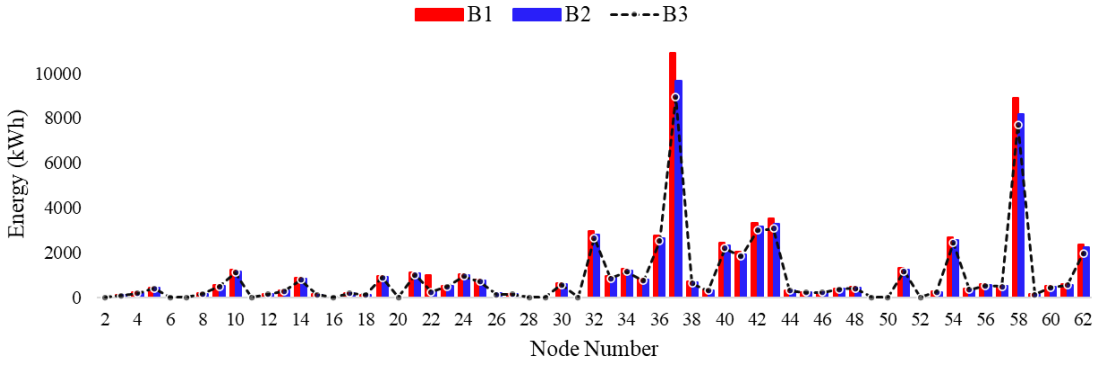

(a) FLS at each node

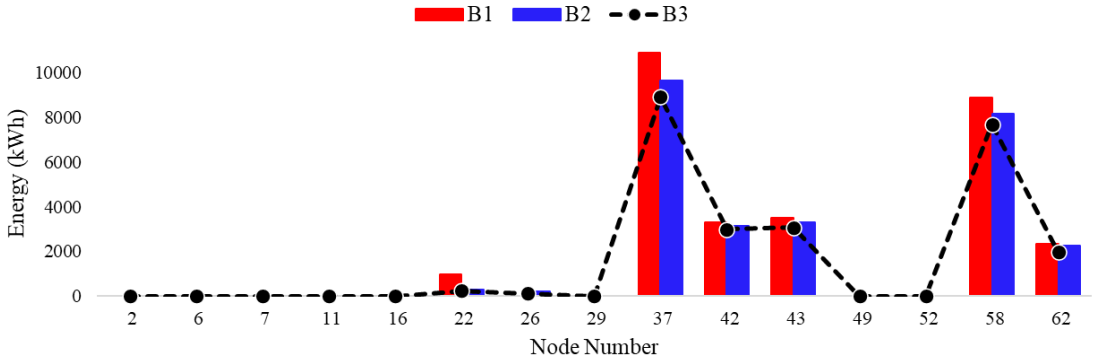

(b) FLS at critical loads

Fig. 11. The rate of FLS in Cases B1-B3

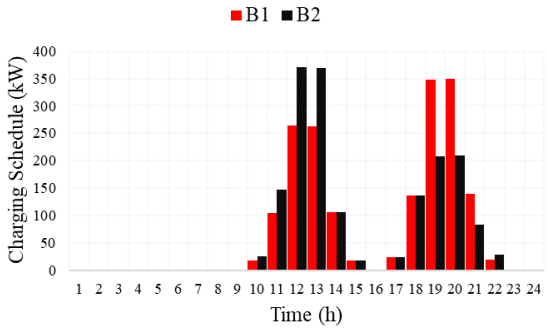

(a) EVCS connected to node 5

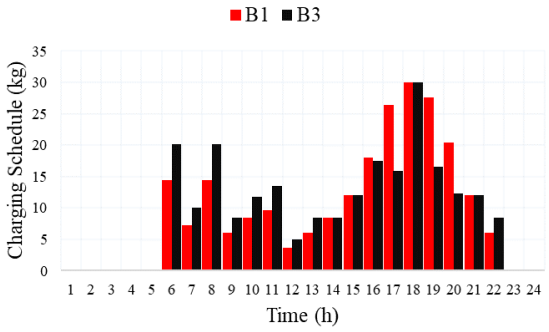

(b) HRS connected to node 18

Fig. 12. Programs obtained for an EVCS and an HRS in Cases B1 & B3

5-4- Results of Cases C1 & C2

In C1, MEESs are included in the self-healing planning process. The results presented in Table 6 indicate that the presence of MEESs has resulted in a 2.91% reduction in costs attributed to FLS.

It is assumed that MEESs are fully charged at the depot and dispatched to the network's connection points after a fault occurs. Figure 13 compares the supply curve of critical network loads in B3 and C1. As shown, the load supply curves align from 1:00 to 14:00; however, from 15:00 onward, the curve rises in C1. It should be noted that the travel time and connection of MEESs to the connection nodes take between 25 to 35 minutes, depending on the distance of the connection points from the depots. In general, it is evident that the network load supply curve significantly increases once the MEESs are connected at 15:00.

In C2, MFCTs are also incorporated into the self-healing planning process and dispatched to connection points by SGO during emergency situations. The results in Table 6 show that the presence of both MEES and MFCTs in self-healing planning reduces the costs related to FLS by 6.69% compared to B3. It is assumed that MFCTs are empty of hydrogen when the fault occurs. Therefore, SGO must first send them to the HRS location to load the purchased hydrogen and then dispatch them to the connection points. Note that the travel and loading time of MFCTs is considered to be 40-50 minutes, depending on the destination of HRSs from the depots. Figure 14 compares the load supply curve in A1-B3, demonstrating that as more parties are activated in the self-healing planning process, more load is supplied. The results also confirm that in C2, where all smart prosumers and mobile units are active in planning, the network load is fully supplied from 15:00 to 16:00 (when all the MFCTs are connected to connection points). Figure 15 illustrates the resulting schedule for MEES and MFCTs in C2. According to this figure, two MEESs are connected to nodes 54 and 60 at 15:00, while one MEES is connected to node 32 at 16:00. It can also be observed that the MFCTs first traveled from the depot to the HRS located in nodes 18 and 61 and then connected to nodes 19 and 60 at 15:00.

Finally, to assess the accuracy and efficiency of the proposed adaptive ADMM algorithm, the results obtained from it are compared with the standard version of the ADMM algorithm, as well as the centralized method. It is important to note that in the centralized method, a comprehensive objective function is defined for self-healing planning, encompassing both SGO planning and the internal planning of smart prosumers. This function aims to minimize all daily costs simultaneously, and its solution is globally optimal. Therefore, the ADMM algorithm's solution is globally optimal only if it matches the solution obtained through the centralized method. Figures 16a and 16b depict the convergence processes related to solving C2 with both the proposed standard and adaptive versions of the ADMM. As evident from these figures, both versions have successfully reached the same solution as the centralized method. Therefore, both versions have achieved the global optimum solution. A comparison of the convergence processes of the algorithms reveals that the proposed adaptive algorithm has converged with 115 fewer iterations, leading to a 34.27% reduction in solution time. Consequently, the results affirm that the proposed adaptive ADMM algorithm not only attains the global optimum solution but also significantly reduces the solution time.

Table 6. Results of Case C1 & C2

Case C1								
Entity	Expenses during Event ($)							
	Components	MEESs	HRSs	LC	FLS	Exchange	Reward	Sum
SG	303.2	189	13781.01	80569.64	31009.22	21342.67	147194.74	303.2
Energy Hubs	1735.66	-	14531.59	-	-7208.33	-20071.26	-11012.34	1735.66
EVCSs	47.93	-	840.64	-	168.54	-1206.09	-148.98	47.93
HRSs	26.14	-	47.75	-	-417.68	-65.32	-409.11	26.14
Case C2								
Entity	Components	MEESs	HRSs	LC	FLS	Exchange	Reward	Sum
SG	303.2	455.11	13781.01	76517.27	30987.75	21291.31	143335.65	303.2
Energy Hubs	1735.23	-	14507.98	-	-7206.37	-20038.64	-11001.8	1735.23
EVCSs	47.93	-	827.58	-	168.54	-1187.35	-143.3	47.93
HRSs	-37.86	-	47.75	-	-417.68	-65.32	-473.11	-37.86

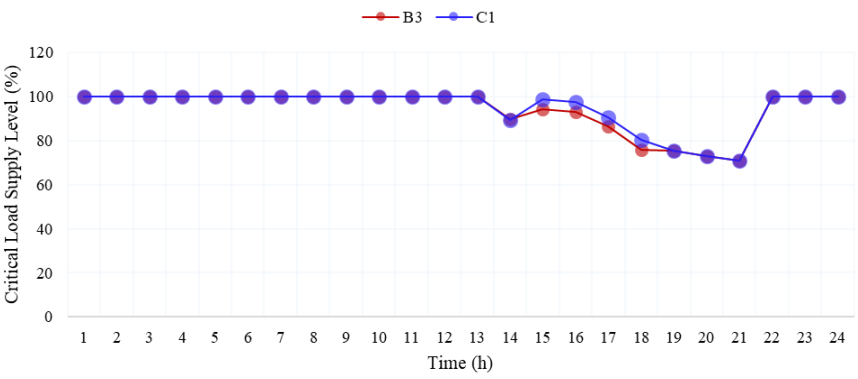

Fig. 13. Critical load supply curve in Cases B3 and C1

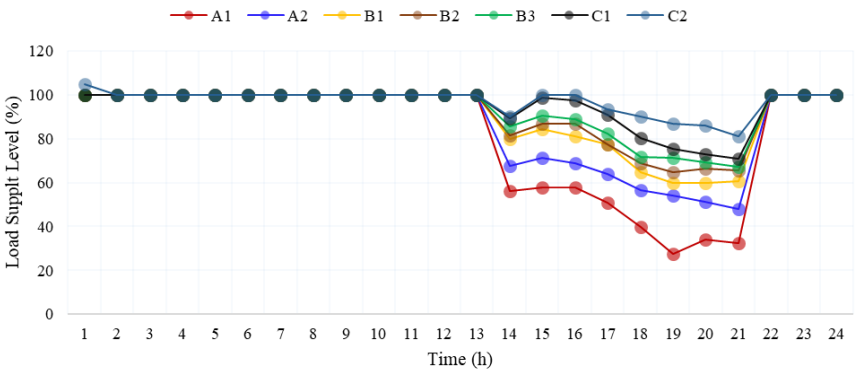

Fig. 14. Load supply curve in all cases

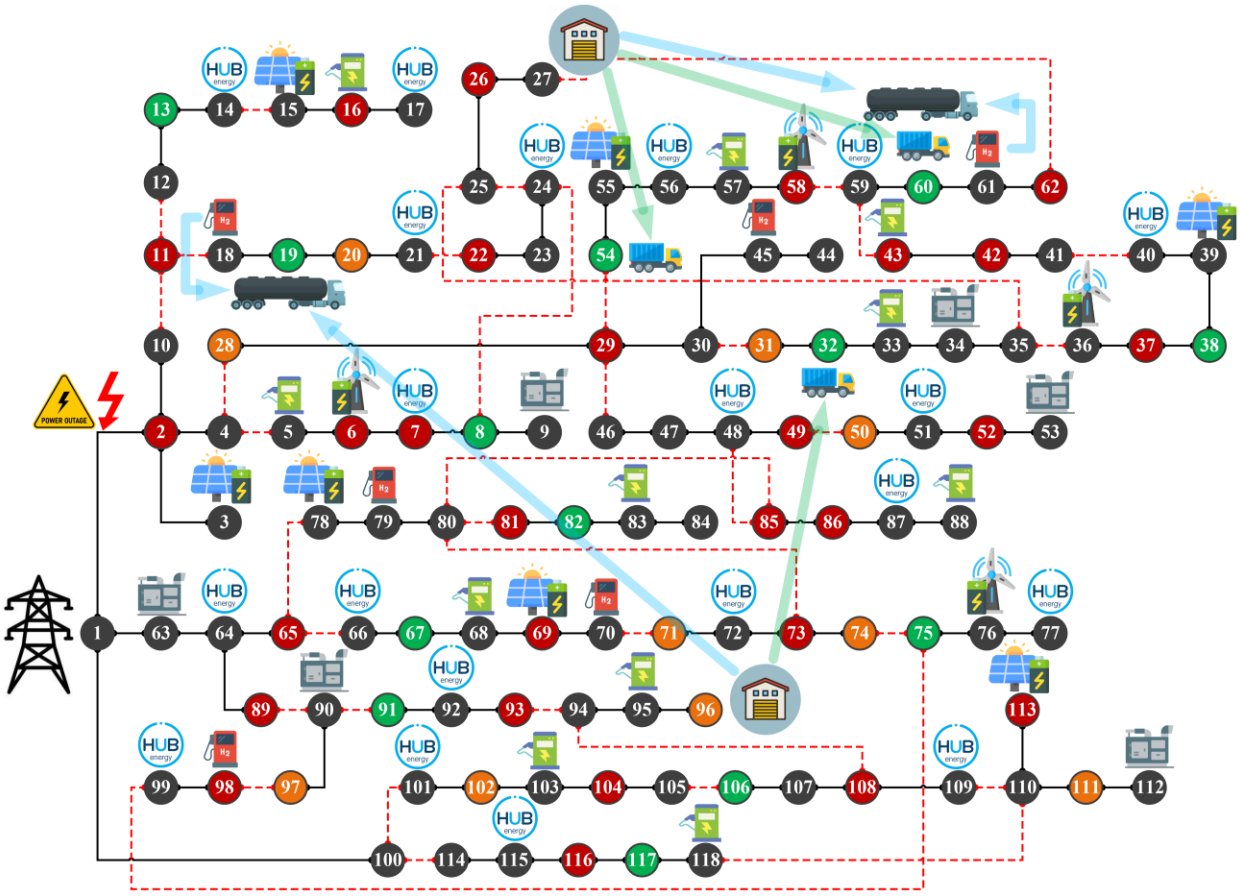

Fig. 15. Programs obtained for MEESs and MFCTs in Case C2

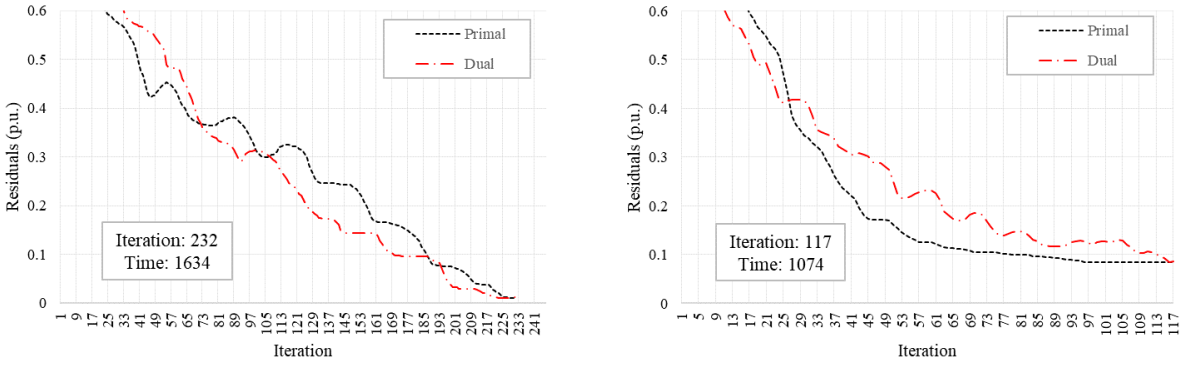

(a) Standard ADMM (b) Proposed adaptive ADMM

Fig. 16. Convergence of the standard and adaptive versions of the ADMM algorithm

6- Conclusion

This paper introduces a bi-level strategy to enhance the self-healing capabilities of smart grids by maximizing the adaptable capacities of smart prosumers and mobile units. The strategy involves two levels: the initial focusing on SGO planning, and the subsequent level addressing smart prosumer planning, including energy hubs, EVCS, and HRS. Each entity pursues its own unique objective function, employing an adaptive ADMM to ensure decentralized optimization. The main findings of the proposed strategy are:

- Our case studies showed that implementing the LC program during emergencies not only significantly reduced FLS at critical loads but also lowered SGO planning costs by 27.99%, highlighting SGO's ability to supply a substantial portion of critical loads during emergencies through LC implementation.
- Simulation results confirmed that energy hubs could contribute significant capacities to SGO by applying an LC mechanism to their loads. Moreover, EVCSs and HRSs could provide substantial capacities to SGO by adjusting the charging schedules of EVs and FCVs. Numerical findings indicated that the simultaneous participation of energy hubs, EVCSs, and HRSs in self-healing planning reduced FLS by 32.04% and SGO costs by 17.48%.
- The simulations also validated that deploying MEES and MFCTs to connection points during emergencies reduced FLS by 6.69% and self-healing costs by 4.02%. Additionally, SGO demonstrated effective coordination in planning MFCTs under its purview by utilizing the proposed mechanism.

- Lastly, our results emphasized that the proposed adaptive ADMM algorithm achieved an optimal solution, comparable to the centralized method, with 115 fewer iterations than the standard version, resulting in a 34.27% reduction in solution time.

Below are implications for further investigation in the field:

1- Develop multi-block ADMM to facilitate parallel decentralized coordination among the transmission system, smart grid, and smart prosumers during emergencies.

2- Develop energy management models to harness the potential of thermostatically controlled loads during emergencies.

3- Investigate the potential of internet data centers to provide fast and reliable balancing services for smart grids during emergencies.

Acknowledgement

The research is supported by the Natural Science Foundation of China (12201001), the Natural Science Foundation of Anhui Province (2108085QA17), and the Natural Science Foundation of Universities of Anhui Province (KJ2020A0009).

References

[1] Fan D, Ren Y, Feng Q, Liu Y, Wang Z, Lin J. Restoration of smart grids: Current status, challenges, and opportunities. Renew Sustain Energy Rev 2021;143:110909. https://doi.org/https://doi.org/10.1016/j.rser.2021.110909.

[2] Qays MO, Ahmad I, Abu-Siada A, Hossain ML, Yasmin F. Key communication technologies, applications, protocols and future guides for IoT-assisted smart grid systems: A review. Energy Reports 2023;9:2440–52. https://doi.org/https://doi.org/10.1016/j.egyr.2023.01.085.

[3] Lee J, Razeghi G, Samuelsen S. Generic microgrid controller with self-healing capabilities. Appl Energy 2022;308:118301. https://doi.org/10.1016/j.apenergy.2021.118301.

[4] Moradi S, Zizzo G, Favuzza S, Massaro F. A stochastic approach for self-healing capability evaluation in active islanded AC/DC hybrid microgrids. Sustain Energy, Grids Networks 2023;33:100982. https://doi.org/https://doi.org/10.1016/j.segan.2022.100982.

[5] Wasiak I, Szypowski M, Kelm P, Mieński R, Wędzik A, Pawełek R, et al. Innovative energy management system for low-voltage networks with distributed generation based on prosumers' active participation. Appl Energy 2022;312:118705. https://doi.org/https://doi.org/10.1016/j.apenergy.2022.118705.

[6] Yin X, Ye C, Ding Y, Song Y. Exploiting Internet Data Centers as Energy Prosumers in Integrated Electricity-Heat System. IEEE Trans Smart Grid 2023;14:167–82. https://doi.org/10.1109/TSG.2022.3197613.

[7] Mansouri SA, Maroufi S, Ahmarinejad A. A tri-layer stochastic framework to manage electricity market within a smart community in the presence of energy storage systems. J Energy Storage 2023;71:108130. https://doi.org/https://doi.org/10.1016/j.est.2023.108130.

[8] Rizeakos V, Bachoumis A, Andriopoulos N, Birbas M, Birbas A. Deep learning-based application for fault location identification and type classification in active distribution grids. Appl Energy 2023;338:120932. https://doi.org/https://doi.org/10.1016/j.apenergy.2023.120932.

[9] Sadeghi M, Kalantar M. Fully decentralized multi-agent coordination scheme in smart distribution restoration: Multilevel consensus. Appl Energy 2023;350:121606. https://doi.org/https://doi.org/10.1016/j.apenergy.2023.121606.

[10] Aguero JR. Applying self-healing schemes to modern power distribution systems. 2012 IEEE Power Energy Soc Gen Meet 2012. https://doi.org/10.1109/pesgm.2012.6344960.

[11] Rath S, Nguyen LD, Sahoo S, Popovski P. Self-Healing Secure Blockchain Framework in Microgrids. IEEE Trans Smart Grid 2023:1. https://doi.org/10.1109/tsg.2023.3253723.

[12] Guan L, Chen H, Lin L. A Multi-Agent-Based Self-Healing Framework Considering Fault Tolerance and Automatic Restoration for Distribution Networks. IEEE Access 2021;9:21522–31. https://doi.org/10.1109/access.2021.3055284.

[13] Costa GB, Damiani JS, Marchesan G, Morais AP, Bretas AS, Cardoso Jr. G. A multi-agent approach to distribution system fault section estimation in smart grid environment. Electr Power Syst Res 2022;204:107658. https://doi.org/10.1016/j.epsr.2021.107658.

[14] Abdelhamid AM, Zakzouk NE, El Safty S. A Multi-Agent Approach for Self-Healing and RES-Penetration in Smart Distribution Networks. Mathematics 2022;10:2275. https://doi.org/10.3390/math10132275.

[15] Nejad RR, Sun W. Enhancing Active Distribution Systems Resilience by Fully Distributed Self-Healing Strategy. IEEE Trans Smart Grid 2022;13:1023–34. https://doi.org/10.1109/TSG.2021.3127518.

[16] Shen F, Wu Q, Xu Y, Li F, Teng F, Strbac G. Hierarchical service restoration scheme for active distribution networks based on ADMM. Int J Electr Power Energy Syst 2020;118:105809. https://doi.org/https://doi.org/10.1016/j.ijepes.2019.105809.

[17] Lv C, Liang R, Chai Y. Decentralized Bilateral Risk-based Self-healing Strategy for Power Distribution Network with Potentials from Central Energy Stations. J Mod Power Syst Clean Energy 2023;11:179–90. https://doi.org/10.35833/MPCE.2022.000436.

[18] Shen F, Lopez JC, Wu Q, Rider MJ, Lu T, Hatziargyriou ND. Distributed Self-Healing

Scheme for Unbalanced Electrical Distribution Systems Based on Alternating Direction Method of Multipliers. IEEE Trans Power Syst 2020;35:2190–9. https://doi.org/10.1109/tpwrs.2019.2958090.

[19] Yeganehkia MH, Rezaei MM, Abedi M, Dowlatshahi M. Presenting a new IGDT-based scheme for risk-based developing of distribution system restoration using online islanding method. Sustain Energy, Grids Networks 2023;34:101014. https://doi.org/10.1016/j.segan.2023.101014.

[20] Zhao Y, Lin J, Song Y, Xu Y. A Hierarchical Strategy for Restorative Self-Healing of Hydrogen-Penetrated Distribution Systems Considering Energy Sharing via Mobile Resources. IEEE Trans Power Syst 2023;38:1388–404. https://doi.org/10.1109/tpwrs.2022.3172968.

[21] Shen Y, Qian T, Li W, Zhao W, Tang W, Chen X, et al. Mobile energy storage systems with spatial–temporal flexibility for post-disaster recovery of power distribution systems: A bilevel optimization approach. Energy 2023;282:128300. https://doi.org/10.1016/j.energy.2023.128300.

[22] Li B, Chen Y, Wei W, Huang S, Xiong Y, Mei S, et al. Routing and Scheduling of Electric Buses for Resilient Restoration of Distribution System. IEEE Trans Transp Electrif 2021;7:2414–28. https://doi.org/10.1109/TTE.2021.3061079.

[23] Dong J, Zhu L, Dong Q, Kritprajun P, Liu Y, Liu Y, et al. Integrating Transactive Energy Into Reliability Evaluation for a Self-Healing Distribution System With Microgrid. IEEE Trans Sustain Energy 2022;13:122–34. https://doi.org/10.1109/tste.2021.3105125.

[24] Bagherzadeh L, Shayeghi H, Pirouzi S, Shafie-khah M, Catalão JPS. Coordinated flexible energy and self-healing management according to the multi-agent system-based

restoration scheme in active distribution network. IET Renew Power Gener 2021;15:1765–77. https://doi.org/10.1049/rpg2.12145.

[25] Vita V, Fotis G, Pavlatos C, Mladenov V. A New Restoration Strategy in Microgrids after a Blackout with Priority in Critical Loads. Sustainability 2023;15:1974. https://doi.org/10.3390/su15031974.

[26] Liu Y, Weng Y, Yang R, Tran Q-T, Nguyen HD. Gaussian process-based bilevel optimization with critical load restoration for system resilience improvement through data centers-to-grid scheme. Sustain Energy, Grids Networks 2023;34:101007. https://doi.org/10.1016/j.segan.2023.101007.

[27] Li Z, Xu Y, Wang P, Xiao G. Coordinated preparation and recovery of a post-disaster Multi-energy distribution system considering thermal inertia and diverse uncertainties. Appl Energy 2023;336:120736. https://doi.org/10.1016/j.apenergy.2023.120736.

[28] Nazar MS, Jafarpour P, Shafie-khah M, Catalão JPS. Optimal planning of self-healing multi-carriers energy systems considering integration of smart buildings and parking lots energy resources. Energy 2023:128674. https://doi.org/10.1016/j.energy.2023.128674.

[29] Alasvand Javadi E, Joorabian M, Barati H. A bi-level optimization framework for resilience enhancement of electricity and natural gas networks with participation of energy hubs. Int J Electr Power Energy Syst 2022;142:108312. https://doi.org/https://doi.org/10.1016/j.ijepes.2022.108312.

[30] Hemmati R, Mehrjerdi H, Nosratabadi SM. Resilience-oriented adaptable microgrid formation in integrated electricity-gas system with deployment of multiple energy hubs. Sustain Cities Soc 2021;71:102946. https://doi.org/https://doi.org/10.1016/j.scs.2021.102946.

[31] Huang W, Zhang X, Li K, Zhang N, Strbac G, Kang C. Resilience Oriented Planning of Urban Multi-Energy Systems With Generalized Energy Storage Sources. IEEE Trans Power Syst 2022;37:2906–18. https://doi.org/10.1109/tpwrs.2021.3123074.

[32] Mansouri SA, Rezaee Jordehi A, Marzband M, Tostado-Véliz M, Jurado F, Aguado JA. An IoT-enabled hierarchical decentralized framework for multi-energy microgrids market management in the presence of smart prosumers using a deep learning-based forecaster. Appl Energy 2023;333:120560. https://doi.org/https://doi.org/10.1016/j.apenergy.2022.120560.

[33] Mansouri SA, Nematbakhsh E, Ahmarinejad A, Jordehi AR, Javadi MS, Marzband M. A hierarchical scheduling framework for resilience enhancement of decentralized renewable-based microgrids considering proactive actions and mobile units. Renew Sustain Energy Rev 2022;168:112854. https://doi.org/10.1016/j.rser.2022.112854.

[34] Aguado JA, Paredes Á. Coordinated and decentralized trading of flexibility products in Inter-DSO Local Electricity Markets via ADMM. Appl Energy 2023;337:120893. https://doi.org/https://doi.org/10.1016/j.apenergy.2023.120893.

[35] Honarmand HA, Shamim AG, Meyar-Naimi H. A robust optimization framework for energy hub operation considering different time resolutions: A real case study. Sustain Energy, Grids Networks 2021:100526. https://doi.org/https://doi.org/10.1016/j.segan.2021.100526.